Solar-wind structure

Solar-wind structure

Mathew Owens

March 3, 2020

Summary:
The hot solar atmosphere continually expands out into space to form the solar wind, which drags with it the Sun's magnetic field. This creates a cavity in the interstellar medium, extending far past the outer planets, within which the solar magnetic field dominates. While the physical mechanisms by which the solar atmosphere is heated are still debated, the resulting solar wind can be readily understood in terms of the pressure difference between the hot, dense solar atmosphere and the cold, tenuous interstellar medium. This results in an accelerating solar-wind profile which becomes supersonic long before it reaches Earth orbit. The large-scale structure of the magnetic field carried by the solar wind is that of an Archimedean spiral, owing to the radial solar-wind flow away from the Sun and the rotation of the magnetic footpoints with the solar surface. Within this relatively simple picture, however, is a range of substructure, on all observable time and spatial scales. Solar-wind flows are largely bimodal in character. "Fast" wind comes from open magnetic field regions, which have a single connection to the solar surface. "Slow" wind, on the other hand, appears to come from the vicinity of closed magnetic field regions, which have both ends connected to the Sun. Interaction of fast and slow wind leads to patterns of solar-wind compression and expansion which sweep past Earth. Within this relatively stable structure of flows, huge episodic eruptions of solar material further perturb conditions. At the smaller scales, turbulent eddies create unpredictable variations in solar wind conditions. These solar-wind structures are of great interest as they give rise to space weather that can adversely affect space- and ground-based technologies, as well as pose a threat to humans in space.

Keywords:
Heliosphere, solar wind, heliospheric magnetic field, corotating interaction regions, stream interaction regions, coronal mass ejections, space weather

1 Introduction

The solar wind is a continual, pressure-driven outflow of plasma from the solar corona - the Sun's hot, extended atmosphere [14]. The solar wind carves out the heliosphere, a solar-controlled bubble in interstellar space that extends far past the outer planets. The out-flowing solar-wind plasma drags with it the

coronal magnetic field to form the heliospheric magnetic field which is central to the interaction of the solar and planetary magnetic fields, a core element of space weather [3], as well as providing the only stellar magnetic field which we can directly measure.

The solar wind exhibits structure on a range of spatial and temporal scales. Most fundamentally, it is observed to be bi-modal in nature. "Fast" wind emanates from large open coronal magnetic regions in which the field is only connected to the Sun at one end. These appear dark in ultraviolet emission and are consequently referred to as coronal holes. (An introduction to coronal structure is provided in [38]).“Slow" wind, on the other hand, originates from near closed coronal magnetic loops, in a region called the streamer belt which is bright in ultraviolet emission. Thus the solar-wind structure in the heliosphere is largely ordered by the magnetic field configuration in the corona.

Confluence of fast and slow winds in the heliosphere leads to large-scale stream interaction regions of compressed solar wind. Within this quasi steady-state flow pattern, huge episodic eruptions of solar plasma and magnetic field known as coronal mass ejections [30] produce transient disturbances which drive the most severe space weather. On the smaller scales, the solar wind exhibits turbulence and coherent structures which may provide insight into the as-yet-undetermined processes by which the corona is heated.

Observations of the solar wind are relatively limited. Direct measurements can be taken at a single point in space by heliospheric spacecraft, but these observations essentially constitute a single slice through a large, evolving solar wind structure. As a result, it is not generally possible to disentangle spatial and temporal variations within the solar wind. Remote, synoptic measurements of solar-wind density structures are possible through both scattered white-light imaging [19] and radio-based techniques [48]. However, these are line-of-sight integrated measurements, often with complex response functions, meaning interpretation in terms of structured, three-dimensional features is difficult, particularly without any magnetic field information for context. Measurements of the magnetic field itself are limited to remote-sensing observations at the solar surface and extremely sparse sampling in the heliosphere via single-point measurements. Thus theoretical extrapolations and modelling, as discussed below, are essential to our interpretation of the available observations and hence understanding of the three-dimensional structure of solar wind.

2 An expanding solar atmosphere

The solar corona is a high electrical conductivity and low-beta plasma, which means that the magnetic pressure is high relative to the thermal pressure [38, 68]. Consequently, coronal dynamics are dominated by the evolution of the coronal magnetic field. In turn, the coronal magnetic field configuration is primarily set by plasma motions in the photosphere where the coronal field is anchored at one or both ends. The coronal plasma is heated to temperatures in excess of 1-2 million Kelvin by magnetic processes which are still under debate [14].

Both the deposition of energy into the plasma by magnetic waves launched from photospheric motions and wide-spread magnetic reconnection (see [68]) in the form of "nanoflares" provide explanations which are broadly consistent with the available observations [14].

But even without understanding why the corona is hot, it can be insightful to consider the implications of a hot solar atmosphere. A hydrostatic atmosphere [13] would require finite constant pressure at large distances from the Sun. The cold tenuous interstellar medium, far from the Sun, would be unable to balance such a pressure, rendering the hydrostatic solution unphysical. Instead, it was proposed that the high coronal temperature results in the continual pressure-driven expansion of solar atmosphere, termed the solar-wind solution [65]. This can be understood by considering radial (r) momentum conservation in the presence of the pressure and gravitational gradients between the hot corona and the cold, tenuous interstellar medium:

$$\rho v_r \frac{dv_r}{dr} = -\frac{dp}{dr} - \rho \frac{GM}{r^2} \tag{1}$$

where v_r is the radial plasma expansion speed, p is the scalar pressure, ρ is the plasma density, G is the universal gravitation constant and M is the solar mass. Mass conservation in spherical geometry gives:

$$\frac{d}{dr}\left[r^2 \rho v_r\right] = 0 \tag{2}$$

To close the set of equations, an equation of state is needed to relate ρ and p. The simplest form is to assume an isothermal corona (though more sophisticated assumptions do not greatly affect the result):

$$p = \rho R T_0 \tag{3}$$

where R is the ideal gas constant and T_0 is the constant coronal temperature. Combining these three equations results in:

$$\frac{1}{v_r}\left[v_r^2 - c_s^2\right] = 2\frac{c_s^2}{r^2}\left[r - r_c\right] \tag{4}$$

where c_s is the isothermal sound speed (i.e., $c_s = \sqrt{RT_0}$) and r_c is the critical radius at which $v_r = c_s$ (i.e., $r_c = GM/2c_s^2$). This equation has a number of possible solutions, however all but one are unphysical as representations of the corona, due to either supersonic flow at the base of the corona, the outflow not beginning at the base of the corona, or finite pressure as $r \to \infty$. The remaining solar-wind solution is shown in Figure 1 for a range of coronal temperatures.

This flow becomes supersonic (strictly speaking, super-magnetosonic, the highest plasma-wave speed) far before it reaches Earth orbit (1 AU). For a coronal temperature of $\approx$ 1MK, the estimated 1-AU solar-wind speeds are in general agreement with the observed values, as discussed in Section 4.

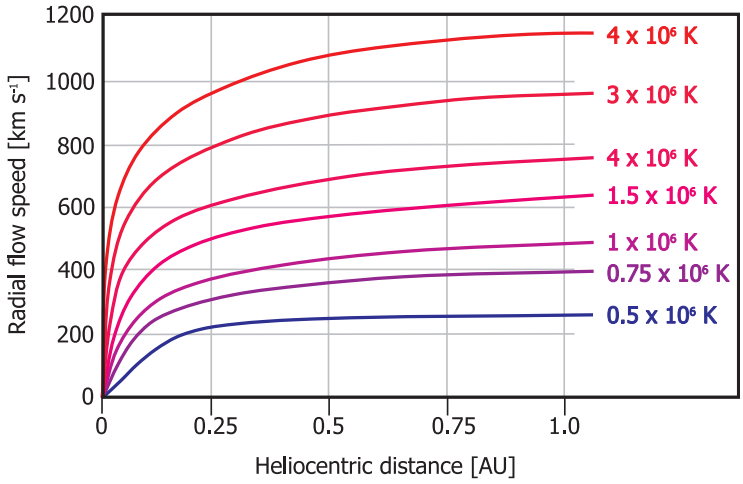

Figure 1: Solutions to the Parker solar-wind equation (described in Section 2) for a range of coronal temperature and heliocentric distance, in astronomical units (AU). Adapted from [65].

3 Coronal and heliospheric magnetic field

3.1 Open solar flux

The Parker solution to the solar-wind outflow described in the previous section assumes that there are no impediments (other than gravity) to the escape of hot coronal plasma, resulting in a uniform solar-wind flow in the heliosphere. Where coronal magnetic flux is "open" to the heliosphere, this is a reasonable approximation. But in general, a static magnetic field will form closed loops which act to restrict the outflow. Indeed, in the low corona the high plasma beta means magnetic pressure exceeds flow momentum, and coronal loops are able to confine the hot plasma in this region. Higher in the solar atmosphere, as the solar-wind flow momentum increases and the magnetic field becomes weaker, a point is reached, referred to as the "source surface", where coronal dynamics are no longer magnetically dominated. Instead, the solar-wind flow drags the coronal magnetic field out so that previously closed loops become "open" and add to the heliospheric magnetic field (HMF). The HMF pervades the solar system and defines the extent of the Sun's magnetic influence, or "heliosphere", as discussed further in Section 8. The integrated coronal magnetic flux which contributes to the HMF (i.e., the total coronal flux which threads the source surface) is termed the "open solar flux" (OSF). The magnitude of the (unsigned) OSF is determined primarily by the strength of the Sun's dipolar magnetic field component [90], as it falls off more slowly with distance from the Sun than the higher-order magnetic field moments.

The implications of a solar wind outflow on a dipolar coronal field was con-

sidered by [67] using a numerical magnetohydrodynamic (MHD) model. They began with a dipolar magnetic field and added a Parker-like solution of a uniform solar wind with speed increasing with coronal altitude. The results are summarised in Figure 2. The dipole field gives near-radial field at the poles, with an increasing weak radial magnetic field component towards the equator. If OSF is defined as the flux which reaches the outer boundary of the simulation domain, equivalent to a source surface around 2-2.5 solar radii, the dipole OSF (shown by the black lines) is limited to the polar regions. Adding the solar-wind flow has little effect on this dipole OSF, though the field lines do become more radial at the simulation outer boundary. The largest effect, however, is for the solar wind to drag out the highest closed loops (red) to generate additional OSF. At the photosphere, this extends the OSF boundary equatorward, though still only a fraction of the total photospheric area is associated with OSF and the equatorial regions remain closed (blue). At the outer edge of the simulation domain, the solar wind outflow produces an increasingly radial field at all altitudes, consistent with source surface at 2-3 solar radii where the field is entirely radial. At the source surface over the equator, the solar-wind flow draws together the legs of a previously closed loop, thus a current sheet will form to separate these opposite magnetic polarities [68]. In three dimensions, this will form a flat disc encircling the Sun. The extension of this current sheet out to the heliosphere, the heliospheric current sheet (HCS, [78]), is discussed further in Section 3.3. The closed loops and draped open flux at the magnetic equator are reminiscent of bright, elongated structures seen in the white-light corona known as "helmet streamers" [38], discussed below.

A global estimate of the coronal and heliospheric magnetic field can be routinely obtained from the remotely measured photospheric field [32], though a number of assumptions and approximations must be made. In particular, as photospheric magnetic field observations are currently made exclusively from near-Earth space, longitudinal coverage of the photosphere requires a full solar rotation of approximately 27 days as viewed from Earth. The polar fields are also difficult to observe from the ecliptic plane and thus are typically "filled in" using lower latitude observations. Once a full synoptic map of the photospheric magnetic field has been obtained, extrapolation to the source surface (normally fixed around 2 to 2.5 solar radii) can be achieved with the Potential-Field Source-Surface (PFSS) model [74, 1], which assumes zero current density in the corona. This effectively results in a static reconstruction of the lowest energy state of the coronal magnetic field. Similarly, photospheric magnetograms can be used as the inner boundary condition to three-dimensional numerical magnetohydrodynamic (MHD) models of the corona [52, 86, 94]. In general, this produces qualitatively similar results to PFSS solutions [72]. The artificial construct of a spherical source surface is not explicitly required in the MHD approach, with the OSF is taken as the radial magnetic flux at the outer boundary of the simulation domain, normally located at 20-30 solar radii, well outside the magnetosonic point.

Observationally, the majority of the OSF is found to be rooted in coronal holes, dark regions in extreme ultraviolet and soft X-ray emission [15]. Figure

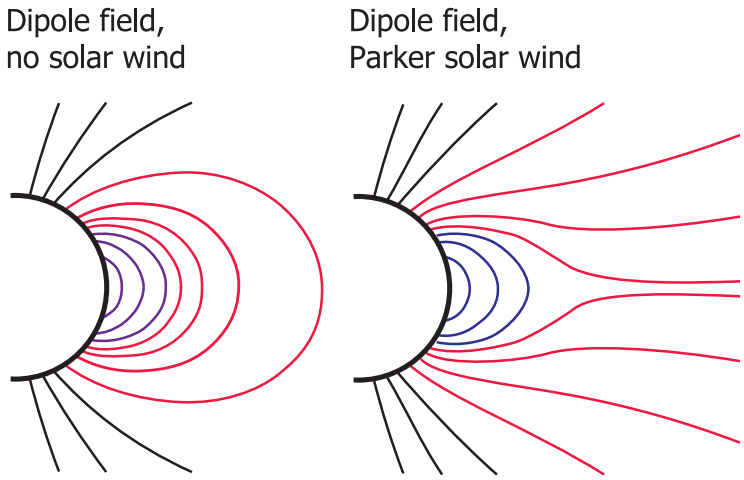

Figure 2: A summary of the numerical experiment by [67]. Left: Magnetic field lines resulting from a purely dipolar coronal magnetic field, with no solar wind outflow. Right: Magnetic field lines resulting from the dipolar field embedded with a Parker-like solar wind outflow (uniform flow, increasing speed with radial distance). Black/blue lines show flux which is open/closed in both cases. Red lines show flux opened by the solar wind outflow.

3 shows the comparison between the photospheric footpoints of OSF, as determined by photospheric magnetic field extrapolation, and observed coronal holes for one solar rotation at solar minimum. There is generally a strong correlation (see, however, [44] for discussion of OSF outside of coronal holes). Both coronal holes and OSF are primarily polar features at this time, consistent with an underlying dipolar configuration to the solar magnetic field. In both the observed coronal holes and model OSF there are two large equatorward extensions, one extending up from the south pole around 0 to 45° longitude, the other extending down from the north pole between 180 and 270°. This indicates a higher-order component to the solar magnetic field, likely resulting from the mid-latitude active regions seen as bright features in the EUV intensity.

The lack of EUV emission within coronal holes is interpreted as a lack of hot material, consistent with the coronal plasma being freely able to escape into space along the open magnetic flux tubes. Conversely, the closed field regions are bright in EUV as the hot plasma is (partially) trapped on closed magnetic loops. In Figure 3, the coronal holes and OSF regions are coloured by the polarity of the magnetic field within them. It can be seen that these are large-scale unipolar regions. As in the [67] simulation, the total photopsheric surface area contributing to the OSF is relatively small, of the order 20%. This suggests considerable non-radial expansion of the OSF between the photosphere and the source surface, where (by definition) the entire sphere is covered by OSF.

The OSF can also be thought of as the component of the total solar field

carried out by the solar wind to form the heliospheric magnetic field (HMF). The *Ulysses* spacecraft [92] made *in-situ* observations of the HMF over a range of heliographic latitudes. *Ulysses* observed that the magnitude of the radial field, B_r, when scaled for distance (i.e., $r^2|B_r|$), is invariant with latitude [79]. As suggested by the [67] simulation, this is contrary to the expectation of a dipolar field configuration, which would exhibit decreasing $|B_r|$ towards the magnetic equator. The latitudinal invariance in $|B_r|$ is consistent with the near-Sun coronal magnetic field undergoing significant non-radial expansion, which acts to equilibrate tangential magnetic pressure (and hence $|B_r|$) on the solar wind source surface [84]. This result means also that a single-point measurement of B_r in the heliosphere is, in principle, sufficient to estimate the total (unsigned) OSF [46].

The degree of non-radial expansion undergone by coronal flux tubes between the photosphere and source surface can vary considerably depending on the depth of the photospheric foot point within a coronal hole. If a flux tube is deep within a coronal hole, it will undergo relatively little non-radial expansion, whereas if it is near the edge of a coronal hole, it will undergo a great deal of non-radial expansion in order to balance tangential magnetic pressure. Where OSF from different coronal holes (or different regions of the same coronal hole) converge, a helmet streamer is produced, as shown schematically in Figure 4. Large helmet streamers are produced when OSF from coronal holes of opposite polarity converge [57, 38]. Thus helmet streamers will contain the sunward edge of the HCS which encircles the Sun. Streamers therefore form a "belt" around the Sun. Smaller "pseudostreamers" [91] are instead observed to be produced where flux from coronal holes of the same polarity converge.

These structures are well reproduced by photospheric magnetic field extrapolations. Figure 5 shows examples of the MAS model solutions to the observed photospheric magnetic field at solar minimum (left) and solar maximum (right). At solar minimum, the photospheric field is relatively simple (see also [87]). There is one large sunspot group of high field intensity near the equator at around 270°longitude, but otherwise the photospheric field is dominated by the large-scale unipolar regions over the poles, consistent with a strong, rotationally aligned dipole. Consequently, open flux is confined almost exclusively to the polar regions, with closed flux over the mid-latitude and equatorial regions. At the source surface (or model outer boundary, in this case), the magnitude of B_r is relatively constant, while the polarity is primarily determined by hemisphere. Consequently, the HCS is located very close to the solar equator. As suggested in Figure 4, the flux from the polar coronal-hole boundary must undergo a great deal of non-radial expansion to extend down from above 50° latitude at the photosphere, to the equator at the source surface. This forms a large-scale streamer belt overlying the solar equator.

At solar maximum, the situation is very different. The photospheric B_r is dominated by mid-latitude active regions, with only a minor polar contribution (and of the same polarity at both poles in this particular example). The resulting coronal holes cover a smaller photospheric area than at solar minimum, and are spread over a range of latitudes. At the source surface, the hemispheric ordering

of B_r has disappeared, and the associated HCS extends from approximately +40 to -90 degrees latitude.

3.2 Parker spiral

The ideal Parker solar-wind solution – of a steady-state solar wind with an exactly radial outflow of constant speed – can be used to give a useful picture of the underlying geometry of the HMF beyond the source surface. A steady-state solution for the HMF can be obtained by assuming the coronal magnetic field is static and rotates rigidly with the Sun (the corona is observed to rotate approximately rigidly, despite the differential rotation of the photosphere [81]). The HMF is frozen in to solar-wind plasma flow [68], and exerts little force on the plasma relative to the flow momentum. As a result, the passive HMF is twisted into an Archimedean spiral, often referred to as the "Parker spiral", and shown schematically in Figure 6. Thus:

$$\frac{B_\phi(r,\theta,\phi)}{B_r(r,\theta,\phi)} = \frac{v_\phi(r,\theta,\phi)}{v_r} = \frac{-\Omega r \sin\theta}{v_r} \tag{5}$$

where B_ϕ is the azimuthal component of the HMF, v_r is the radial solar-wind speed (for simplicity, assumed to be constant above the source surface), v_ϕ is the azimuthal solar-wind speed and θ is the latitude being considered. v_ϕ results from the frame of reference rotation at angular speed Ω, the mean coronal rotation speed. The $\sin\theta$ term is due to the decreasing rotation speed of the source-surface footpoint from equator to pole. Thus B_ϕ exhibits a $1/r$ fall off with distance:

$$B_\phi(r,\theta,\phi) = -B_r(r_0,\theta,\phi_0)\frac{\Omega r_0^2 \sin\theta}{v_r r} \tag{6}$$

The assumption of purely radial solar-wind flow at the source surface means that the meridional component of the HMF, B_θ, is zero at all locations.

The angle of the Parker spiral HMF to the radial direction, $\gamma_P = \arctan(B_\phi/B_r)$, is thus a function of heliocentric distance, heliographic latitude and solar wind speed. At a given heliographic latitude θ, the HMF is wrapped around the surface of a cone with half angle θ. Thus for a given v_r and r, γ_P decreases with latitude, with the purely radial HMF originating at the rotational pole. (Note that in the non-rotating frame of reference, all velocity streamlines are radial but the HMF remains the same.) For a solar-wind speed of 400 km s^{-1}, typical of near-Earth space, γ_P is approximately 45° in the ecliptic plane at 1 AU.

These predictions of the large-scale HMF were confirmed by the first *in-situ* spacecraft observations of the near-Earth HMF [55], both in terms of γ_P and the confinement, on average, to the solar equatorial plane. Indeed, the Parker model has been shown to provide a good approximation of the observed HMF over a wide range of distances from the Sun: from Helios observations in the inner heliosphere [7] to the distant outer heliosphere [9]. *Ulysses* observations provided comprehensive latitudinal sampling and observed close agreement with the Parker spiral, including the general unwinding of the spiral at higher latitudes [23], and, on average, no net B_θ component.

Figure 7 shows the occurrence of observed γ_P as a function of solar wind speed using hourly measurements from near-Earth space over the period 1965-2018. The HMF "unwinds" and becomes more radial at higher speeds, as expected. The vertical dashed lines show the equivalent ideal Parker spiral values, in agreement with the mean values of the observations. However, it is clear that the Parker spiral only describes the behaviour of the HMF in an average sense: There are frequent large deviations from the Parker spiral direction on the hourly timescale.

3.3 Magnetic sector structure

Open solar flux consists of equal amounts of inward and outward HMF. Close to the heliographic equator, such as in near-Earth space, an observer will see an alternating pattern of inward and outward HMF as the Sun rotates and the HCS sweeps past. If the coronal magnetic field is not evolving significantly on the solar rotation time scale (27 days, as viewed from Earth), this pattern will be quasi-periodic [4]. This "magnetic sector structure" is shown in Figure 8, both from *in-situ* near-Earth observations and extrapolated from the photospheric magnetic field observations using the PFSS model. In both cases the black line shows the observed HCS location. In general, the two approaches are in close agreement.

Around the declining phase of the solar cycle and during solar minimum, when the Sun's magnetic field is dominated by the dipolar component, a 2-sector structure (i.e., one interval of inward and one interval of outward HMF polarity per solar rotation) is most commonplace. However, even at solar minimum the remaining quadrupole (and higher-rder) moments are still sometimes sufficient to distort the HCS and produce more complex HMF sector patterns (e.g., four sector structure) in the ecliptic plane. This is consistent with the solar-minimum source surface B_r shown in Figure 5, where the HCS has a small amplitude wave pattern of order 2 or 3, which could result in multiple sectors in near-Earth space, depending on the heliographic latitude of Earth at that time.

Observations out of the ecliptic plane are far less frequent. The *Ulysses* spacecraft was in a polar orbit of the Sun and made three "fast latitude scans" wherein it travelled from the southern to northern pole of the Sun in approximately one year. In addition to comprehensively sampling heliographic latitude, solar rotation means *Ulysses* also sampled solar longitude. If the coronal structure is assumed to be relatively constant over a year, this allows a synoptic map of the solar wind conditions to be constructed [35], as shown by the centre and right panels of Figure 9. At solar minimum, the distribution of HMF polarity is hemispherically determined, with the HCS (and hence the streamer belt) close to the heliographic equator. At solar maximum, the *Ulysses* observations suggest a magnetic dipole that is orthogonal to the rotational axis. However, this assumes no significant coronal evolution over the year taken to scan in latitude, which is likely to be invalid at solar maximum. Instead of providing an instantaneous snap shot of the polarity of the HMF, the time variation in the latitude of *Ulysses* and of the HMF is likely resulting in aliasing in the map. Nevertheless,

	Coronal hole	Streamer belt
V_r	750 km s^{-1}	300-400 [km s^{-1}]
n_P	2-4 cm^{-3}	5-10 cm^{-3}
T_P	2-3 $\times 10^5$ K	0.5-1 $\times 10^5$ K
$\|B\|$	3-4 nT	4-8 nT
T_O	1.1 $\times 10^6$K	1.6 $\times 10^6$K
T_C	1 $\times 10^6$K	1.4 $\times 10^6$K
Fe:O	0.07	0.08-0.1
Si:O	0.1	0.13-0.16

Table 1: Typical properties of coronal-hole and streamer-belt solar wind. Parameters are: V_r, radial solar-wind speed; n_P, proton number density; T_P, proton temperature; $|B|$, magnetic field intensity; T_O, effective coronal temperature from the *in situ* oxygen charge-state ratio; T_C, effective coronal temperature from the *in situ* carbon charge-state ratio; Fe:O, the iron to oxygen abundance ratio; and Si:O, the silicon to oxygen abundance ratio. The first four parameters evolve with distance from the Sun and so have been scaled to 1-AU values.

it is still qualitatively similar to the solar maximum interval shown in Figure 5.

4 Fast and slow solar wind

In-situ spacecraft observations, particularly from outside the ecliptic plane, reveal two fundamental forms of solar wind. As shown by the right-hand panels of Figure 9, at solar minimum the *Ulysses* spacecraft observed fast wind ($\approx$ 750 km s^{-1}) over the polar regions and much slower wind ($\approx$ 400 km s^{-1}) over the equatorial regions. These two distinct types of wind are clearly associated with different coronal magnetic field configurations. The fast wind is associated with open solar flux which originates from coronal holes. The slow solar wind maps to latitudes associated with the closed magnetic flux and the streamer belt (e.g., Figure 5). Thus while the terms "fast" and "slow" wind are widely used, it is more accurate to refer to coronal-hole and streamer-belt wind: speed measured *in situ* is the result of both initial conditions at the source surface and subsequent heliospheric processes between the source surface and observer. Furthermore, the difference between coronal hole and streamer belt wind extends well beyond typical speed, as will be detailed below.

Table 1 compares typical properties of coronal-hole and streamer-belt wind, scaled to 1 AU (see, *e.g.* [18] for more detail). In general, the coronal-hole wind is fast, tenuous and containing relatively weak HMF. The streamer-belt wind tends to be more variable, though is slower, denser and contains stronger HMF than the coronal hole wind.

Using a PFSS model of the corona, [89] found an anti-correlation between the amount of non-radial flux-tube expansion from the photosphere to the source surface, and the observed solar wind speed. This relation has since been refined

[72] to include the depth of an open-flux footpoint into a coronal hole and is the basis of a number of solar-wind forecast methods [2]. The solar-wind speed obtained from such empirical relations to static coronal magnetic field topology is shown in the bottom panels of Figure 5. Comparison with the *Ulysses* solar-wind speed observations (Figure 9) show good qualitative agreement. At solar minimum, coronal hole wind dominates, with streamer belt wind confined to a narrow equatorial region; at solar maximum slow wind dominates, with coronal hole wind confined to small isolated pockets. It is important to note, however, that while coronal flux tube expansion acts as a good proxy for solar-wind speed, it is unlikely to be the physical mechanism (though the Bernoulli theorem of fluid dynamics would indeed predict a decrease in laminar flow speed with the decrease in fluid pressure of an expanding flow channel cross-sectional area). Evidence for different coronal release mechanisms comes from elemental composition and ion charge-state measurements made *in situ*. Unlike solar-wind speed, temperature, density and HMF properties, composition and ion-charge states are fixed in the corona and are unaffected by subsequent coronal processes.

The high conductivity of the solar wind means cross-magnetic field diffusion of particles is severely inhibited [69] and hence different plasma regimes on different HMF flux tubes cannot mix efficiently. Thus elemental-abundance ratios of the solar wind are largely unchanged from their coronal source values. Similarly, the collisionless nature of the solar wind means ion-electron recombination does not routinely occur, and ion charge-states are fixed by the electron temperature back in the corona where the plasma was last collisional [64]; higher ion-charge states in the solar wind are indicative of hotter coronal source regions. These properties therefore give unique insight into the coronal source properties of different types of solar wind.

Figure 10 shows the average variation in elemental composition and ion-charge states as the solar wind transitions from fast, coronal-hole wind (day -13 to 0), to slow, streamer-belt wind (day 0 to 13). Firstly, it is clear that the transition is difficult to identify in solar-wind speed alone, but is readily apparent in the coronal source properties. Indeed, on days -13 and 0 there is relatively slow coronal hole wind, while around days 1 and 13 there is relatively fast streamer belt wind. Coronal hole wind is easily identifiable by the bias towards low first-ionisation potential (FIP) elements, in close agreement with the composition of the photosphere. Conversely, streamer-belt wind contains a greater proportion of high-FIP elements, suggesting a chromospheric source [40]. Similar trends are present in the ion-charge state ratios, shown as the equivalent coronal temperatures in Figure 10. Coronal-hole wind is consistent with a relatively cool coronal source, while streamer-belt wind suggests higher coronal-source temperatures, consistent with hot coronal loops [88].

5 Stream interaction regions

The solar dipole axis is typically inclined with respect to the rotational axis. Even when this inclination is small, the quadrupole and higher-order compo-

nents of the solar magnetic field mean that the coronal magnetic field (and hence solar-wind speed structure) is not azimuthally symmetric. Longitudinal variation in solar-wind speed coupled with solar rotation results in radial gradients in solar wind speed. This results in compression, deflection and momentum transfer of the interacting solar-wind streams.

Figure 11 shows a schematic of the interaction between a fast and slow solar wind stream. Fast wind catches up with slow wind ahead of it and the resulting stream interface (SI) takes the form of a spiral front in the heliosphere. The surrounding region of compressed and deflected solar wind, bounded by the forward and reverse waves, is the stream interaction region (SIR). Behind the SIR, the fast wind will move away from the trailing slow wind. This results in a rarefaction region, which can lead to near-radial HMF in near-Earth space [34]. If the coronal magnetic field does not significantly evolve over the period of a solar rotation, the SIR will approximately corotate with the Sun. In near-Earth space, such corotating interaction regions (CIRs) [66, 26] are particularly prevalent during the declining phase of the solar cycle, when the corona can both be approximated as steady-state and the magnetic axis has a relatively large inclination to the rotation axis.

An example of a stream interaction region is shown in Figure 12. Slow, streamer-belt wind is compressed and accelerated by the forward shock, resulting in elevated speed, density and magnetic field intensity. Similarly, fast, coronal-hole wind is slowed and compressed by the reverse wave, which has not steepened into a shock in this case. The expected bipolar flow deflection, from positive (in the solar rotation direction) to negative (against the solar rotation direction) is clear in V_ϕ between the forward and reverse waves. The stream interface, between the accelerated streamer belt wind and the decelerated coronal hole wind, is best identified by oxygen- and carbon-ion charge states. High ion-charge states indicate high coronal source temperatures, which are unaffected by the stream interaction processes. Also shown in Figure 12 is the angle of the HMF to the radial direction, ϕ_B, which shows that the HMF polarity reversal associated with the passage of the HCS is embedded within the SIR. The HCS is within the streamer-belt wind and thus gets swept up by the forward wave and precedes the SI.

A more general picture of the solar wind properties around the HCS is presented in Figure 13. It presents the median variations for 5 days either side of 307 HCS crossings [85] observed by the *Advanced Composition Explorer* (ACE) spacecraft [82] in near-Earth space. As shown in the third panel of Figure 8, the HCS is typically embedded in the slow, dense solar wind. While the density increase will be at least partly the result of in-transit compression from solar-wind stream interaction, the ion-charge states also indicate the plasma around the HCS originates in the hot corona. The HCS is also associated with enhanced occurrence of high FIP elements (see also [6]). This is all consistent with slow solar-wind release from the vicinity of helmet streamers, as shown in Figure 9. The HCS typically precedes a modest enhancement in HMF, the result of compression by the associated solar-wind speed gradient. Note that the compression also leads to a deflection of orientation of the HMF, with the

out-of-ecliptic component of the HMF, B_Z, contributing a larger fraction of the total HMF in the compressed region.

6 Solar-wind transients

Despite resulting from time-dependent processes such as rotation and solar-wind acceleration, the coronal and solar-wind structures described above are best described as steady state, in that they can be largely understood in terms of a static coronal magnetic field in the corotating frame. Conversely, the coronal transients discussed in this section are associated with dynamic coronal magnetic field structures and are episodic in nature.

6.1 Non-Parker HMF

The Parker spiral is a very successful description of the average HMF. In order to fully describe the available observations, however, refinements to the model are needed, which in turn have implications for solar-wind formation and release mechansims.

One observation not immediately explainable by the Parker spiral HMF is the existence of shock-accelerated particles at heliographic latitudes much greater than accessible by the SIRs which produce them [73]. This either requires energetic particles to undergo strong diffusion perpendicular to the HMF [39] or for HMF flux tubes to span a range of latitudes, contrary to the ideal Parker spiral. The latter can be achieved by changing the photospheric connectivity of the HMF footpoint. Along lines of constant latitude, this process must occur in order for the corona to rotate rigidly while the photosphere rotates differentially. Magnetic reconnection between the open flux and a closed loop, known as interchange reconnection [17, 16], allows the open flux footpoint to "hop" from one leg of the closed loop to the other. By continual interchange reconnection at the edge of coronal holes, they can rigidly rotate with a period of approximately 25 days at all latitudes [54]. Equivalent motion of HMF in latitude was proposed by [21] to explain both existence of shock-accelerated particles at high latitudes and the release of hot plasma from coronal loops to form the slow wind [22]. An associated decline in solar-wind speed at the HMF footpoint [75] results in systematically more radial HMF in the rarefaction region behind SIRs than the ideal Parker spiral predicts.

Further support for the time-dependent nature of the slow solar wind comes from energetic electron observations. Suprathermal electrons have energies above the thermal plasma and thus stream along the HMF, carrying the heat flux away from the Sun [20]. With distance from source surface, the suprathermal electrons become focussed into a narrow beam, known as the "strahl", which is ever present in the solar wind and serves as an effective tracer of HMF topology and connectivity to the Sun. As the strahl is always moving out from the hot coronal source, under ideal Parker-spiral conditions it will be parallel to the HMF in outward polarity sectors, and anti-parallel to the the HMF in

inward polarity sectors. However, the converse is occasionally observed, suggesting that locally the strahl is moving sunward. This is the result of inverted or folded HMF [36], likely the result of interchange reconnection in the corona opening up a previously closed coronal loop. Inverted HMF has the plasma and ion charge-state properties of the slow wind and is observed to originate from the vicinity of dipolar- and pseudo-streamers [63], suggesting slow solar wind is released by interchange reconnection. The variable, time-dependent nature of the slow solar wind is discussed further in Section 7.

6.2 Interplanetary coronal mass ejections

The largest-scale solar transients are coronal mass ejections (CMEs), episodic eruptions of solar plasma and magnetic field [30]. In the heliosphere, the interplanetary manifestations of CMEs (ICMEs) can be measured *in situ* and are found to result in the largest deviations from the steady-state Parker solar wind. They are the primary source of strong out-of-ecliptic (i.e., meridional) HMF. As a result, ICMEs drive the most extreme space weather [25].

ICMEs are distinct from "ambient" solar wind (i.e., coronal-hole and streamer-belt solar wind) in a number of ways, though there is a great deal of event-to-event variability within ICMEs and no one signature is always present. In many ICMEs, magnetic field intensity is enhanced, while plasma pressure is lower than the bulk solar wind, suggesting ICMEs undergo magnetically driven expansion [11]. This is frequently observed *in situ* in the form of a smoothly declining radial-speed profile, as shown in Figure 14. Ion-charge states and elemental abundances are generally closer to the streamer-belt than coronal-hole wind and, in many cases, CMEs display signatures consistent with hotter coronal-source regions than even the streamer-belt wind, suggesting further heating possibly from associated solar flares [97].

In the corona, CMEs display a wide range of speeds, from $\approx$ 100 km s s^{-1}, to $>$ 3000 km s^{-1} [95]. ICMEs in near-Earth space, however, are observed with a narrower range of speed, typically 250 km s^{-1} to 1000 km s^{-1} [11]. This convergence towards ambient solar-wind speeds is consistent with aerodynamic drag of the ambient solar wind acting on the ejecta [12]. Thus a large fraction of CMEs start with higher speeds than the ambient solar wind in which they're embedded. Furthermore, the radial expansion of ICMEs means that the ICME leading edge is typically moving faster than the centre of mass, as shown in Figure 14. Thus ahead of ICMEs there is frequently a region of compressed and deflected ambient solar wind, called the ICME sheath, which is bounded by the ICME leading edge and the bow wave. For the fastest ICMEs, the bow wave will steepen into a shock.

Figure 14 shows an example of an ICME observed by the ACE spacecraft in near-Earth space. The ICME is moving much faster than the ambient solar wind (an average speed of around 750 km s^{-1}, compared with the $\approx$ 600 km s^{-1} upstream). Additionally, the ICME is expanding in the radial direction, resulting in the leading-edge speed of nearly 900 km s^{-1} and a trailing-edge speed just below the ambient solar-wind speed. This results in compression of the ambient

solar wind both ahead and behind the ICME, though it is much stronger ahead. As illustrated here, the upstream ICME sheath region associated with an event typically contains the fastest solar-wind speeds, highest densities and some of the strongest magnetic field intensities. The ion charge-states and elemental composition, however, show that the sheath is compressed ambient solar wind, rather than of different coronal origin. Conversely, the ICME contains highly elevated oxygen charge states, suggesting a very hot coronal source. As a result, elevated ion charges states are one of the most robust signatures in identifying a subset of ICMEs [43]. Similarly, the high FIP elements are enhanced, at least during the leading portion of the ICME. This particularly ICME contains a highly ordered magnetic field structure. The field direction smoothly rotates, consistent with a magnetic flux rope passing the spacecraft [37, 42]. These "magnetic clouds" make up somewhere between a quarter and a half of all ICMEs observed in near-Earth space [71], though whether all CMEs begin life with a magnetic flux-rope structure and the signature is lost due to in-transit processes or sampling effects is still a subject of debate.

Within around half of all ICMEs observed in near-Earth space, the suprathermal electron strahl is observed both parallel and antiparallel to the HMF [77]. This "counterstreaming electron" signature suggests the ICME magnetic flux consists of newly emerged closed loops with both ends still connected to the hot corona [27]. Thus the global picture of ICME is of a curved flux-rope, as shown in Figure 15. This picture has important consequences for the relation between the HMF and CMEs; as new OSF can only be produced by dragging a previously closed coronal loop through the source surface and in to the heliosphere, CMEs are a major source of OSF production [59], as well as the means by which the corona sheds excess twist in the magnetic field [47].

7 Small-scale solar-wind structure

At smaller spatial and temporal scales, the solar wind continues to be highly structured, displaying a range of wave phenomena, shocks, turbulence and discontinuities [8, 33]. These processes result in a spectrum of fluctuations in the HMF observed throughout the heliosphere. Coronal hole wind is particularly dominated by Alfvénic fluctuations, flowing anti-sunward in the solar-wind frame [80]. The implications of turbulence in terms of the heating of the corona is discussed in [14].

A stationary spacecraft, e.g. in near-Earth space, measures temporal variability in the HMF as spatial structures resulting from turbulent eddies and waves convect past. It has, however, also been argued that a significant proportion of the observed solar-wind and HMF variability could be the result of structures convected from the corona by the solar wind [5]. In this description, the largest changes in the magnetic field direction result from crossing boundaries between large, coherent flux tubes of coronal origin, while the smaller fluctuations result from true turbulent fluctuations within the flux tubes themselves. Large-angle HMF changes are observed on average every 10 minutes,

suggesting spatial scales in approximate agreement with super-granules on the Sun [56]. Small-scale coronal "blobs" of plasma density have been observed in the vicinity of the heliospheric current sheet [76], suggesting the slow solar wind is composed of a series of intermittent transient events, as opposed tog a smooth, continuous outflow of material. However, the weak association between large magnetic discontinuities and compositional changes [62] mean they are equally as likely to have formed by turbulence during transit, as to be of solar origin.

Regardless of origin, magnetic field discontinuities in the solar wind are typically the result of a shear in the HMF direction, a necessary condition for magnetic reconnection [68]. Conversely, the relatively high plasma beta somewhat inhibits widespread reconnection in the solar wind. Outflow exhausts resulting from reconnection are now routinely observed in the near-Earth solar wind [28]. The leading edge of fast ICMEs is a preferential location for reconnection, as different flow regimes converge, but reconnection is not always highly driven and appears to also regularly occur at low HMF shear angles in low plasma beta fields, often within ICMEs themselves [29].

8 Global heliosphere

Until recently, the outer boundary of the solar wind was understood purely from a theoretical and modelling standpoint [96]. Recently, however, it has been possible to both directly sample [31] and remotely image [50] the structures at the interface between the solar wind and interstellar medium.

The gross morphology of the global heliosphere is sketched in Figure 16. The heliosphere is moving relative to the local interstellar medium (LISM) at around 23 km s^{-1} [45]. Uncertainty in the LISM magnetic field intensity and orientation means that there is still uncertainty about whether this motion is super-magnetosonic and thus results in a standing bow shock within the LISM. Much like the magnetosphere in the solar wind [3], the heliosphere itself is expected to be deformed as a result of the relative motion of the LISM, being compressed on the inflow side and extended on the outflow side. The heliospause, which separates the solar wind and LISM, is therefore expected to be asymmetric. Inside the heliopause, a termination shock is required to slow and deflect the supermagnetosonic solar wind. The distances from the Sun at which the Voyager 1 and 2 spacecraft encountered the termination shock [83] and energetic particle observations made in the vicinity of the termination shock [49] show that it too is non-spherical, as expected.

Inside the termination shock, the HMF of the outer heliosphere is generally well described by the Parker-spiral model [9]. However, the observed latitudinal invariance in $|B_r|$ means $|B|$ in the outer heliosphere should be significantly stronger near the equator than the poles, which is not observed [93]. The explanation is likely related to latitudinal solar-wind speed gradients and the occurrence of SIRs, with excess plasma pressure driving meridional transport of magnetic flux from the equator to higher latitudes [70].

Solar-wind structure in the outer heliosphere is dominated by merged inter-

action regions (MIRs) which form as SIRs and ICMEs converge and coalesce [10]. Like the SIRs and ICMEs that produce them, MIRs are transient structures which produce significant deviations to the ideal Parker-spiral HMF and are expected to produce a significant disturbance to the structure of the heliopause and termination shock.

9 Looking ahead

With increased reliance on space-based technologies, understanding of solar wind structures and the space weather they drive is more important than ever. The sparse nature of *in situ* solar-wind measurements and the complexity of remote-sensing observations mean that theoretical constraints and solar wind modelling are essential to interpreting these data in terms of time-dependent, three-dimensional structures. Simulation sophistication is ever improving in terms of numerical and physical representation. Methods are being developed to rigorously combine observations and models to exploit the strengths of both [41]. However, truly new observations are also expected. *Parker Solar Probe* [24], launched in August 2018, and *Solar Orbiter* [53], due for launch in February 2020, provide unprecedented opportunities to study the "young" solar wind close to the Sun, before it has chance to interact and evolve. *Solar Orbiter* will also provide coordinated *in situ* and remote-sensing observations in an effort to observe both the local solar wind in detail and its coronal-source region. As the mission progresses, *Solar Orbiter* will also reach higher heliographic latitudes, only previously well sampled by the *Ulysses* mission and then at much greater heliocentric distances. At the other end of the system, the heliospheric boundaries will also be probed in greater detail than before with the *Interstellar Mapping and Acceleration Probe* [51], due for launch in 2024. These fresh perspectives will undoubtedly improve our understanding of solar-wind formation and evolution throughout the heliosphere.

References

[1] M. D. Altschuler and G. Newkirk. Magnetic fields and the structure of the solar corona. *Sol. Phys.*, 9:131–149, 1969.

[2] C. N. Arge and V. J. Pizzo. Improvement in the prediction of solar wind conditions using near-real time solar magnetic field updates. *J. Geophys. Res.*, 105:10465, 2000.

[3] C. Arridge. Solar wind - interaction with planets. In B. Foster, editor, *Oxford Research Encyclopedia of Physics*. Oxford University Press, Oxford, 2019.

[4] J. Bartels. Twenty-seven day recurrences in terrestrial-magnetic and solar activity, 1923-1933. *Terrestrial Magnetism and Atmospheric Elec-*

tricity (Journal of Geophysical Research), 39:201, 1934. doi: 10.1029/TE039i003p00201. URL http://10.0.4.5/TE039i003p00201.

[5] J. E. Borovsky. Flux tube texture of the solar wind: Strands of the magnetic carpet at 1 AU? *J. Geophys. Res.*, 113:8110–+, 2008. doi: 10.1029/2007JA012684. URL http://10.0.4.5/2007JA012684.

[6] G. Borrini, J. T. Gosling, S. J. Bame, and W. C. Feldman. Helium abundance variations in the solar wind. *Solar Physics*, 83(2):367–378, 1983. doi: 10.1007/bf00148286. URL https://doi.org/10.1007/BF00148286.

[7] R. Bruno and B. Bavassano. On the winding of the IMF spiral for slow and fast wind within the inner heliosphere. *Geophysical Research Letters*, 24(18):2267–2270, 9 1997. ISSN 00948276. doi: 10.1029/97GL02183. URL http://doi.wiley.com/10.1029/97GL02183.

[8] R. Bruno and V. Carbone. The Solar Wind as a Turbulence Laboratory. *Liv. Rev. Sol. Phys.*, 2:4–+, 2005.

[9] L. F. Burlaga, N. F. Ness, Y.-M. Wang, and N. R. Sheeley. Heliospheric magnetic field strength and polarity from 1 to 81 AU during the ascending phase of solar cycle 23. *J. Geophys. Res.*, 107:1410, 2002. doi: 10.1029/2001JA009217. URL http://10.0.4.5/2001JA009217http://onlinelibrary.wiley.com/store/10.1029/2001JA009217/asset/jgra16391.pdf?v=1&t=i5sb4np5&s=297c72bb0962482bcba5d2c090efc03a08ad453f.

[10] L. F. Burlaga, N. F. Ness, F. B. McDonald, J. D. Richardson, and C. Wang. Voyager 1 and 2 Observations of Magnetic Fields and Associated Cosmic-Ray Variations from 2000 through 2001: 60-87 AU. *Astrophys. J.*, 582:540–549, 2003. doi: 10.1086/344571. URL http://10.0.4.62/344571http://iopscience.iop.org/0004-637X/582/1/540/pdf/0004-637X_582_1_540.pdf.

[11] H. V. Cane and I. G. Richardson. Interplanetary coronal mass ejections in the near-Earth solar wind during 1996-2002. *J. Geophys. Res.*, 108:1156, 2003. doi: 10.1029/2002JA009817. URL http://10.0.4.5/2002JA009817.

[12] P. J. Cargill. On the aerodynamic drag force acting on coronal mass ejections. *Sol. Phys.*, 221:135, 2004.

[13] S. Chapman. Notes on the solar corona and the terrestrial ionosphere. *Smithsonian contributions to astrophysics*, 2(1):1–19, 1957. URL https://repository.si.edu/bitstream/handle/10088/6598/SCAS-0003.pdf.

[14] S. Cranmer. Solar Wind Origin. In B. Foster, editor, *Oxford Research Encyclopedia of Physics*. Oxford University Press, Oxford, 2019.

[15] S. R. Cranmer. Coronal Holes. *Liv. Rev. Sol. Phys.*, 6:3, 2009. doi: 10.12942/lrsp-2009-3. URL http://10.0.50.142/lrsp-2009-3.

[16] N. U. Crooker and M. J. Owens. Interchange Reconnection: Remote Sensing of Solar Signature and Role in Heliospheric Magnetic Flux Budget. *Space Science Reviews*, 172(1-4):201–208, 2 2011. ISSN 0038-6308. doi: 10.1007/s11214-011-9748-1. URL http://link.springer.com/10.1007/s11214-011-9748-1.

[17] N. U. Crooker, J. T. Gosling, and S. W. Kahler. Reducing heliospheric flux from coronal mass ejections without disconnection. *J. Geophys. Res.*, 107, 2002. doi: 10.1029/2001JA000236. URL http://10.0.4.5/2001JA000236.

[18] R. W. Ebert, D. J. McComas, H. A. Elliott, R. J. Forsyth, and J. T. Gosling. Bulk properties of the slow and fast solar wind and interplanetary coronal mass ejections measured by Ulysses: Three polar orbits of observations. *Journal of Geophysical Research: Space Physics*, 114(A1):n/a–n/a, 1 2009. ISSN 01480227. doi: 10.1029/2008JA013631. URL http://doi.wiley.com/10.1029/2008JA013631.

[19] C. J. Eyles, R. A. Harrison, C. J. Davis, N. R. Waltham, B. M. Shaughnessy, H. C. A. Mapson-Menard, D. Bewsher, S. R. Crothers, J. A. Davies, and G. M. Simnett. The heliospheric imagers onboard the STEREO mission. *Sol. Phys.*, 254(2):387–445, 2009.

[20] W. C. Feldman, J. R. Asbridge, S. J. Bame, M. D. Montgomery, and S. P. Gary. Solar wind electrons. *J. Geophys. Res.*, 80:4181–4196, 1975.

[21] L. A. Fisk. Motion of the footpoints of heliospheric magnetic field lines at the Sun: Implications for recurrent energetic particle events at high heliographic latitudes. *J. Geophys. Res.*, 101:15547–15554, 1996. doi: 10.1029/96JA01005. URL http://10.0.4.5/96JA01005http://onlinelibrary.wiley.com/doi/10.1029/96JA01005/abstract.

[22] L. A. Fisk. Acceleration of the solar wind as a result of the reconnection of open magnetic flux with coronal loops. *J. Geophys. Res.*, 108, 2003. doi: 10.1029/2002JA009284. URL http://10.0.4.5/2002JA009284.

[23] R. J. Forsyth, A. Balogh, and E. J. Smith. The underlying direction of the heliospheric magnetic field through the Ulysses first orbit. *Journal of Geophysical Research*, 107(A11):1405, 11 2002. ISSN 0148-0227. doi: 10.1029/2001JA005056. URL http://doi.wiley.com/10.1029/2001JA005056.

[24] N. J. Fox, M. C. Velli, S. D. Bale, R. Decker, A. Driesman, R. A. Howard, J. C. Kasper, J. Kinnison, M. Kusterer, D. Lario, M. K. Lockwood, D. J. McComas, N. E. Raouafi, and A. Szabo. The Solar Probe Plus Mission: Humanity's First Visit to Our Star. *Space Science Reviews*, 204(1-4):7–48, 12 2016. ISSN 0038-6308. doi: 10.1007/s11214-015-0211-6. URL http://link.springer.com/10.1007/s11214-015-0211-6.

[25] J. T. Gosling. The solar flare myth. *J. Geophys. Res.*, 98:18937–18950, 1993. doi: 10.1029/93JA01896. URL http://10.0.4.5/93JA01896.

[26] J. T. Gosling and V. J. Pizzo. Formation and Evolution of Corotating Interaction Regions and their Three Dimensional Structure. *Space Sci. Rev.*, 89:21–52, 1999. doi: 10.1023/A:1005291711900. URL http://10.0.3.255/A:1005291711900.

[27] J. T. Gosling, D. N. Baker, S. J. Bame, W. C. Feldman, and R. D. Zwickl. Bidirectional solar wind electron heat flux events. *J. Geophys. Res.*, 92: 8519–8535, 1987.

[28] J. T. Gosling, R. M. Skoug, D. J. McComas, and C. W. Smith. Magnetic disconnection from the Sun: Observations of a reconnection exhaust in the solar wind at the heliospheric current sheet. *Geophys. Res. Lett.*, 32:L05105, 2005. doi: 10.1029/2005GL022406. URL http://10.0.4.5/2005GL022406.

[29] J. T. Gosling, S. Eriksson, D. J. McComas, T. D. Phan, and R. M. Skoug. Multiple magnetic reconnection sites associated with a coronal mass ejection in the solar wind. *J. Geophys. Res.*, 112:8106–+, 2007. doi: 10.1029/2007JA012418. URL http://10.0.4.5/2007JA012418.

[30] L. Green. Solar Coronal Mass Ejections. In B. Foster, editor, *Oxford Research Encyclopedia of Physics*. Oxford University Press, Oxford, 2019.

[31] D. A. Gurnett, W. S. Kurth, L. F. Burlaga, and N. F. Ness. In Situ Observations of Interstellar Plasma with Voyager 1. *Science*, 341:1489–1492, 2013. doi: 10.1126/science.1241681. URL http://10.0.4.102/science.1241681.

[32] J. T. Hoeksema and P. H. Scherrer. Solar magnetic field, 1976 through 1985: an atlas of photospheric magnetic field observations and computed coronal magnetic fields from the John M. Wilcox Solar Observatory at Sanford, 1976-1985. *NASA STI/Recon Technical Report N*, 86:29760, 1986.

[33] T. S. Horbury, D. Burgess, M. Fränz, and C. J. Owen. Three spacecraft observations of solar wind discontinuities. *Geophys. Res. Lett.*, 28: 677–680, 2001. doi: 10.1029/2000GL000121. URL http://10.0.4.5/2000GL000121.

[34] G. H. Jones, A. Balogh, and R. J. Forsyth. Radial heliospheric magnetic fields detected by Ulysses. *Geophysical Research Letters*, 25(16):3109–3112, 8 1998. ISSN 00948276. doi: 10.1029/98GL52259. URL http://doi.wiley.com/10.1029/98GL52259.

[35] G. H. Jones, A. Balogh, and E. J. Smith. Solar magnetic field reversal as seen at Ulysses. *Geophys. Res. Lett.*, 30:8028, 2003. doi: 10.1029/2003GL017204. URL http://10.0.4.5/2003GL017204.

[36] S. W. Kahler, N. U. Crooker, and J. T. Gosling. The topology of intrasector reversals of the interplanetary magnetic field. *J. Geophys. Res.*, 101:24373–24382, 1996. doi: 10.1029/96JA02232. URL http://10.0.4.5/96JA02232.

[37] L. W. Klein and L. F. Burlaga. Interplanetary magnetic clouds at 1 AU. *J. Geophys. Res.*, 87:613–624, 1982.

[38] J. Klimchuk. Solar Corona. In *Oxford Research Encyclopedia of Physics*. Oxford University Press, Oxford, 2019.

[39] J. Kota and J. R. Jokipii. Corotating Variations of Cosmic Rays Near the South Heliospheric Pole. *Science*, 268:1024–1025, 1995. doi: 10.1126/science.268.5213.1024. URL `http://10.0.4.102/science.268.5213.1024`.

[40] J. M. Laming. The FIP and Inverse FIP Effects in Solar and Stellar Coronae. *Living Reviews in Solar Physics*, 12(1):2, 12 2015. ISSN 2367-3648. doi: 10.1007/lrsp-2015-2. URL `http://link.springer.com/10.1007/lrsp-2015-2`.

[41] M. Lang and M. J. Owens. A Variational Approach to Data Assimilation in the Solar Wind. *Space Weather*, 17(1):59–83, 1 2019. ISSN 15427390. doi: 10.1029/2018SW001857. URL `http://doi.wiley.com/10.1029/2018SW001857`.

[42] R. P. Lepping, J. A. Jones, and L. F. Burlaga. Magnetic field structure of interplanetary clouds at 1 AU. *J. Geophys. Res.*, 95:11957–11965, 1990. doi: 10.1029/JA095iA08p11957.

[43] S. T. Lepri, T. H. Zurbuchen, L. A. Fisk, I. G. Richardson, H. V. Cane, and G. Gloeckler. Iron charge distribution as an identifier of interplanetary coronal mass ejections. *J. Geophys. Res.*, 106(A12):29231–29238, 2001. doi: 10.1029/2001JA000014. URL `http://dx.doi.org/10.1029/2001JA000014`.

[44] J. A. Linker, R. M. Caplan, C. Downs, P. Riley, Z. Mikic, R. Lionello, C. J. Henney, C. N. Arge, Y. Liu, M. L. Derosa, A. Yeates, and M. J. Owens. The Open Flux Problem. *Astrophys. J.*, in press, 2017. doi: 10.3847/1538-4357/aa8a70.

[45] J. L. Linsky, A. Diplas, B. E. Wood, A. Brown, T. R. Ayres, and B. D. Savage. Deuterium and the Local Interstellar Medium Properties for the Procyon and Capella Lines of Sight. *Astrophys. J.*, 451:335, 1995. doi: 10.1086/176223. URL `http://10.0.4.62/176223`.

[46] M. Lockwood, R. J. Forsyth, A. Balogh, and D. J. McComas. Open solar flux estimates from near-Earth measurements of the interplanetary magnetic field: comparison of the first two perihelion passes of the Ulysses spacecraft. *Ann. Geophys.*, 22:1395–1405, 2004.

[47] B. C. Low. Coronal mass ejections, magnetic flux ropes, and solar magnetism. *J. Geophys. Res.*, 106:25141–25160, 2001. doi: 10.1029/2000JA004015.

[48] P. K. Manoharan. THREE-DIMENSIONAL EVOLUTION OF SOLAR WIND DURING SOLAR CYCLES 22-24. *The Astrophysical Journal*, 751 (2):128–141, 2012. doi: 10.1088/0004-637X/751/2/128.

[49] D. J. McComas and N. A. Schwadron. An explanation of the Voyager paradox: Particle acceleration at a blunt termination shock. *Geophys. Res. Lett.*, 33:4102, 2006. doi: 10.1029/2005GL025437. URL `http://10.0.4.5/2005GL025437`.

[50] D. J. McComas, F. Allegrini, P. Bochsler, M. Bzowski, M. Collier, H. Fahr, H. Fichtner, P. Frisch, H. O. Funsten, S. A. Fuselier, G. Gloeckler, M. Gruntman, V. Izmodenov, P. Knappenberger, M. Lee, S. Livi, D. Mitchell, E. Möbius, T. Moore, S. Pope, D. Reisenfeld, E. Roelof, J. Scherrer, N. Schwadron, R. Tyler, M. Wieser, M. Witte, P. Wurz, and G. Zank. IBEX - Interstellar Boundary Explorer. *Space Sci. Rev.*, 146: 11–33, 2009. doi: 10.1007/s11214-009-9499-4. URL `http://10.0.3.239/s11214-009-9499-4`.

[51] D. J. McComas, E. R. Christian, N. A. Schwadron, N. Fox, J. Westlake, F. Allegrini, D. N. Baker, D. Biesecker, M. Bzowski, G. Clark, C. M. S. Cohen, I. Cohen, M. A. Dayeh, R. Decker, G. A. de Nolfo, M. I. Desai, R. W. Ebert, H. A. Elliott, H. Fahr, P. C. Frisch, H. O. Funsten, S. A. Fuselier, A. Galli, A. B. Galvin, J. Giacalone, M. Gkioulidou, F. Guo, M. Horanyi, P. Isenberg, P. Janzen, L. M. Kistler, K. Korreck, M. A. Kubiak, H. Kucharek, B. A. Larsen, R. A. Leske, N. Lugaz, J. Luhmann, W. Matthaeus, D. Mitchell, E. Moebius, K. Ogasawara, D. B. Reisenfeld, J. D. Richardson, C. T. Russell, J. M. Sokół, H. E. Spence, R. Skoug, Z. Sternovsky, P. Swaczyna, J. R. Szalay, M. Tokumaru, M. E. Wiedenbeck, P. Wurz, G. P. Zank, and E. J. Zirnstein. Interstellar Mapping and Acceleration Probe (IMAP): A New NASA Mission. *Space Science Reviews*, 214 (8):116, 12 2018. ISSN 0038-6308. doi: 10.1007/s11214-018-0550-1. URL `http://link.springer.com/10.1007/s11214-018-0550-1`.

[52] Z. Mikic, J. A. Linker, D. D. Schnack, R. Lionello, and A. Tarditi. Magnetohydrodynamic Modeling of the Global Solar Corona. *Phys. Plasma*, 6: 2217, 1999.

[53] D. Müller, R. G. Marsden, O. C. St. Cyr, H. R. Gilbert, and T. S. O. Team. Solar Orbiter. *Solar Physics*, 285(1-2):25–70, 7 2013. ISSN 0038-0938. doi: 10.1007/s11207-012-0085-7. URL `http://link.springer.com/10.1007/s11207-012-0085-7`.

[54] A. G. Nash, N. R. Sheeley, and Y. M. Wang. Mechanisms for the rigid rotation of coronal holes. *Solar Physics*, 117(2):359–389, 1988. ISSN 0038-0938. doi: 10.1007/BF00147253. URL `http://link.springer.com/10.1007/BF00147253`.

[55] M. Neugebauer and C. W. Snyder. Solar plasma experiment. *Science*, 138 (3545):1095–1097, 1962. doi: 10.1126/science.138.3545.1095-a.

[56] M. Neugebauer, B. E. Goldstein, D. J. McComas, S. T. Suess, and A. Balogh. Ulysses observations of microstreams in the solar wind from coronal holes. *J. Geophys. Res.*, 1002:23389–23396, 1995. doi: 10.1029/95JA02723. URL http://10.0.4.5/95JA02723.

[57] G. Newkirk. STRUCTURE OF THE SOLAR CORONA. *Review of Astronomy and Astrophysics*, 5(1):213–266, 1967. URL www.annualreviews.org.

[58] M. J. Owens. DO THE LEGS OF MAGNETIC CLOUDS CONTAIN TWISTED FLUX-ROPE MAGNETIC FIELDS? *The Astrophysical Journal*, 818(2):197, 2 2016. doi: 10.3847/0004-637X/818/2/197. URL http://stacks.iop.org/0004-637X/818/i=2/a=197?key=crossref.c76f07d23f7ef6d60703427a3adbef35.

[59] M. J. Owens and N. U. Crooker. Coronal mass ejections and magnetic flux buildup in the heliosphere. *Journal of Geophysical Research*, 111(A10): 1–8, 10 2006. ISSN 0148-0227. doi: 10.1029/2006JA011641. URL http://centaur.reading.ac.uk/5831/.

[60] M. J. Owens and R. J. Forsyth. The Heliospheric Magnetic Field. *Liv. Rev. Sol. Phys.*, 10:5, 2013. doi: 10.12942/lrsp-2013-5. URL http://10.0.50.142/lrsp-2013-5.

[61] M. J. Owens, N. U. Crooker, and M. Lockwood. How is open solar magnetic flux lost over the solar cycle? *J. Geophys. Res.*, 116(A4):A04111, 2011. doi: 10.1029/2010JA016039. URL http://10.0.4.5/2010JA016039.

[62] M. J. Owens, R. T. Wicks, and T. S. Horbury. Magnetic Discontinuities in the Near-Earth Solar Wind: Evidence of In-Transit Turbulence or Remnants of Coronal Structure? *Sol. Phys.*, 269:411–420, 2011. doi: 10.1007/s11207-010-9695-0. URL http://10.0.3.239/s11207-010-9695-0.

[63] M. J. Owens, N. U. Crooker, and M. Lockwood. Solar origin of heliospheric magnetic field inversions: Evidence for coronal loop opening within pseudostreamers. *J. Geophys. Res.*, 118:1868–1879, 2013. doi: 10.1002/jgra.50259. URL http://10.0.3.234/jgra.50259.

[64] S. P. Owocki, T. E. Holzer, and A. J. Hundhausen. The solar wind ionization state as a coronal temperature diagnostic. *Astrophysical Journal*, 275 (1):354–366, 1983. doi: 10.1086/161538.

[65] E. N. Parker. Dynamics of the interplanetary gas and magnetic fields. *Astrophys. J.*, 128:664–676, 1958.

[66] V. J. Pizzo. The evolution of corotating stream fronts near the ecliptic plane in the inner solar system. II - Three-dimensional tilted-dipole fronts. *J. Geophys. Res.*, 96:5405–5420, 1991. doi: 10.1029/91JA00155. URL http://10.0.4.5/91JA00155.

[67] G. W. Pneuman and R. A. Kopp. Gas-magnetic field interactions in the solar corona. *Solar Physics*, 18(2):258–270, 6 1971. ISSN 0038-0938. doi: 10.1007/BF00145940. URL http://link.springer.com/10.1007/BF00145940.

[68] E. Priest. Solar physics - overview. In B. Foster, editor, *Oxford Encyclopedia of Physics*. Oxford University Press, Oxford, 2019.

[69] E. R. Priest. The basic equations of magnetohydrodynamics. In *Solar Magnetohydrodynamics*. D. Reidel publishing company, 1982.

[70] J. D. Richardson and K. I. Paularena. Meridional flow in the solar wind. *J. Geophys. Res.*, 101:19995–20002, 1996. doi: 10.1029/96JA01715. URL http://10.0.4.5/96JA01715.

[71] P. Riley and I. G. Richardson. Using Statistical Multivariable Models to Understand the Relationship Between Interplanetary Coronal Mass Ejecta and Magnetic Flux Ropes. *Sol. Phys.*, 284(1):217–233, 2013.

[72] P. Riley, J. A. Linker, Z. Mikic, R. Lionello, S. A. Ledvina, and J. G. Luhmann. A Comparison between Global Solar Magnetohydrodynamic and Potential Field Source Surface Model Results. *Astrophys. J.*, 653: 1510–1516, 2006. doi: 10.1086/508565. URL http://10.0.4.62/508565.

[73] E. C. Roelof, G. M. Simnett, R. B. Decker, L. J. Lanzerotti, C. G. Maclennan, T. P. Armstrong, and R. E. Gold. Reappearance of recurrent low-energy particle events at Ulysses/HI-SCALE in the northern heliosphere. *J. Geophys. Res.*, 102:11251–11262, 1997. doi: 10.1029/97JA00640. URL http://10.0.4.5/97JA00640.

[74] K. H. Schatten, J. M. Wilcox, and N. F. Ness. A model of interplanetary and coronal magnetic fields. *Sol. Phys.*, 9:442–455, 1969.

[75] N. A. Schwadron. An explanation for strongly underwound magnetic field in co-rotating rarefaction regions and its relationship to footpoint motion on the the sun. *Geophys. Res. Lett.*, 29:1663, 2002. doi: 10.1029/2002GL015028. URL http://10.0.4.5/2002GL015028.

[76] N. R. Sheeley Jr, T. N. Knudson, and Y.-M. Wang. Coronal inflows and the Sun's nonaxisymmetric open flux. *The Astrophysical Journal Letters*, 546(2):L131, 2001.

[77] S. Shodhan, N. U. Crooker, S. W. Kahler, R. J. Fitzenreiter, D. E. Larson, R. P. Lepping, G. L. Siscoe, and J. T. Gosling. Counterstreaming electrons in magnetic clouds. *J. Geophys. Res.*, 105:27261–27268, 2000.

[78] E. J. Smith. The heliospheric current sheet and modulation of Galactic cosmic rays. *J. Geophys. Res.*, 95:18731–18743, 1990. doi: 10.1029/JA095iA11p18731. URL http://10.0.4.5/JA095iA11p18731.

[79] E. J. Smith and A. Balogh. Ulysses observations of the radial magnetic field. *Geophys. Res. Lett.*, 22:3317–3320, 1995. doi: 10.1029/95GL02826. URL http://10.0.4.5/95GL02826.

[80] E. J. Smith, A. Balogh, M. Neugebauer, and D. McComas. Ulysses observations of Alfvén waves in the southern and northern solar hemispheres. *Geophys. Res. Lett.*, 22:3381–3384, 1995. doi: 10.1029/95GL03268. URL http://10.0.4.5/95GL03268.

[81] G. Stenborg, R. Schwenn, B. Inhester, and N. Srivastava. On the rotation rate of the emission of the solar corona. In A. Wilson, editor, *Magnetic Fields and Solar Processes. The 9th European Meeting on Solar Physics*, page 1107, Florence, 1999. ESA Publications Division. ISBN 9290927925. doi: 1999ESASP.448.1107S. URL http://adsabs.harvard.edu/abs/1999ESASP.448.1107S.

[82] E. Stone, A. Frandsen, R. Mewaldt, E. Christian, D. Margolies, J. Ormes, and F. Snow. The Advanced Composition Explorer. *Space Science Reviews*, 86(1/4):1–22, 1998. ISSN 00386308. doi: 10.1023/A:1005082526237. URL http://link.springer.com/10.1023/A:1005082526237.

[83] E. C. Stone, A. C. Cummings, F. B. McDonald, B. C. Heikkila, N. Lal, and W. R. Webber. An asymmetric solar wind termination shock. *Nature*, 454:71–74, 2008. doi: 10.1038/nature07022. URL http://10.0.4.14/nature07022.

[84] S. T. Suess and E. J. Smith. Latitudinal dependence of the radial IMF component: Coronal imprint. *Geophys. Res. Lett.*, 23:3267–3270, 1996. doi: 10.1029/96GL02908. URL http://10.0.4.5/96GL02908.

[85] S. R. Thomas, M. J. Owens, M. Lockwood, and C. J. Scott. Galactic Cosmic Ray Modulation near the Heliospheric Current Sheet. *Sol. Phys.*, 289(7):2653–2668, 2014. doi: 10.1007/s11207-014-0493-y. URL http://10.0.3.239/s11207-014-0493-y.

[86] G. Tóth, I. V. Sokolov, T. I. Gombosi, D. R. Chesney, C. R. Clauer, D. L. De Zeeuw, K. C. Hansen, K. J. Kane, W. B. Manchester, R. C. Oehmke, K. G. Powell, A. J. Ridley, I. I. Roussev, Q. F. Stout, O. Volberg, R. A. Wolf, S. Sazykin, A. Chan, B. Yu, and J. Kóta. Space Weather Modeling Framework: A new tool for the space science community. *J. Geophys. Res.*, 110:A12226, 2005. doi: 10.1029/2005JA011126. URL http://10.0.4.5/2005JA011126.

[87] L. van Driel-Gesztelyi and M. Owens. The solar cycle. In B. Foster, editor, *Oxford Encyclopedia of Physics*. Oxford University Press, Oxford, 2019.

[88] R. von Steiger, N. A. Schwadron, L. A. Fisk, J. Geiss, G. Gloeckler, S. Hefti, B. Wilken, R. R. Wimmer-Schweingruber, and T. H. Zurbuchen. Composition of quasi-stationary solar wind flows from Ulysses/Solar Wind Ion Composition Spectrometer. *Journal of Geophysical Research: Space Physics*,

105(A12):27217–27238, 2000. doi: 10.1029/1999JA000358. URL https://agupubs.onlinelibrary.wiley.com/doi/abs/10.1029/1999JA000358.

[89] Y.-M. Wang and J. Sheeley, N. R. Solar wind speed and coronal flux-tube expansion. *The Astrophysical Journal*, 355:726, 6 1990. ISSN 0004-637X. doi: 10.1086/168805. URL http://adsabs.harvard.edu/doi/10.1086/168805.

[90] Y.-M. Wang and N. R. Sheeley Jr. Coronal Mass Ejections and the Solar Cycle Variation of the Sun's Open Flux. *The Astrophysical Journal Letters*, 809(2):L24, 2015. doi: 10.1088/2041-8205/809/2/L24.

[91] Y.-M. Wang, R. Grappin, E. Robbrecht, and N. R. Sheeley Jr. On the Nature of the Solar Wind from Coronal Pseudostreamers. *Astrophys. J.*, 749(2):182, 2012. doi: 10.1088/0004-637X/749/2/182. URL http://10.0.4.64/0004-637X/749/2/182.

[92] K. P. Wenzel, R. G. Marsden, D. E. Page, and E. J. Smith. The ULYSSES Mission. *Astron. and Astrophys. Supp.*, 92:207, 1992.

[93] D. Winterhalter, E. J. Smith, J. A. Slavin, and J. H. Wolfe. Spatial gradients in the heliospheric magnetic field - Pioneer 11 observations between 1 AU and 24 AU, and over solar cycle 21. *J. Geophys. Res.*, 95:1–11, 1990. doi: 10.1029/JA095iA01p00001. URL http://10.0.4.5/JA095iA01p00001.

[94] M. S. Yalim, N. Pogorelov, and Y. Liu. A data-driven MHD model of the global solar corona within Multi-Scale Fluid-Kinetic Simulation Suite (MS-FLUKSS). *Journal of Physics: Conference Series*, 837(1): 012015, 5 2017. ISSN 1742-6588. doi: 10.1088/1742-6596/837/1/012015. URL http://stacks.iop.org/1742-6596/837/i=1/a=012015?key=crossref.d155cf706c9ad44a097ad1217a4b5618.

[95] S. Yashiro, N. Gopalswamy, G. Michalek, O. C. St Cyr, S. P. Plunkett, N. B. Rich, and R. A. Howard. A catalog of white light coronal mass ejections observed by the SOHO spacecraft. *J. Geophys. Res.*, 109, 2004. doi: 10.1029/2003JA010282. URL http://10.0.4.5/2003JA010282.

[96] G. P. Zank. Interaction of the solar wind with the local interstellar medium: A theoretical perspective. *Space Sci. Rev.*, 89(3-4):413–688, 1999. doi: 10.1023/A:1005155601277.

[97] T. H. Zurbuchen and I. G. Richardson. In-situ solar wind and magnetic field signatures of interplanetary coronal mass ejections. *Space Sci. Rev.*, 123(1-3):31–43, 2006.

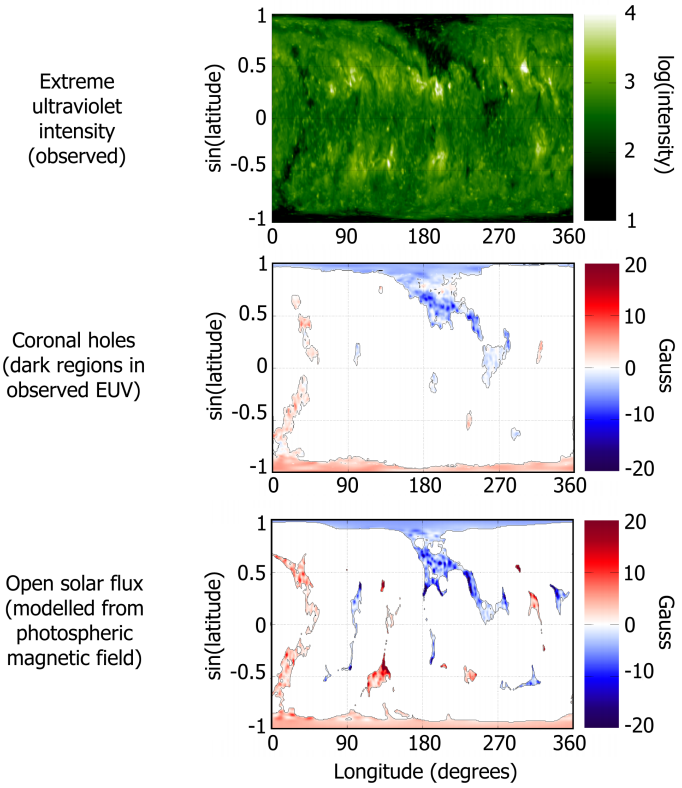

Figure 3: Synoptic (latitude-longitude) maps of the Sun for June/July 2010. Top: The observed extreme ultraviolet (EUV) intensity from the AIA instrument on the Solar Dynamics Observatory (SDO). Middle: Shaded areas indicate coronal holes determined by applying an intensity threshold to the EUV observations. They are coloured red or blue depending on the observed polarity of the photospheric flux within. Bottom: The open flux photospheric footpoints obtained using the MAS coronal model constrained by the observed photospheric magnetic field. Adapted from [44].

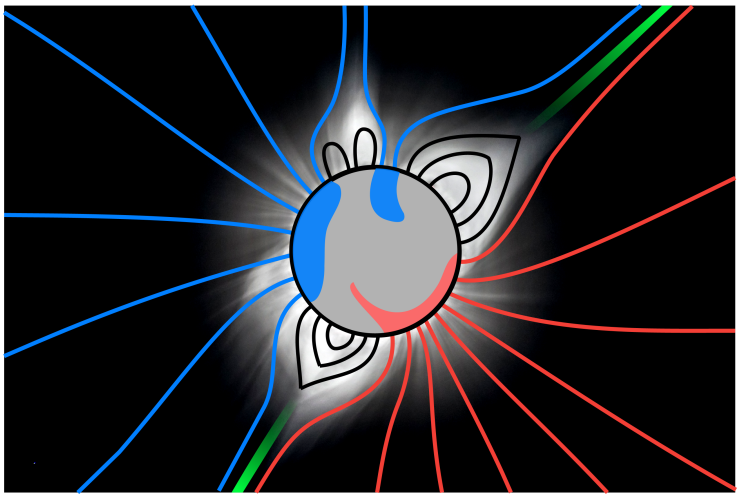

Figure 4: Background: A white-light eclipse image of the corona, with brighter regions indicating higher plasma density. Foreground: A schematic of the coronal magnetic field in the plane of the sky. Blue and red lines show inward and outward polarity open solar flux. The blue and red shaded areas on the solar disk show the associated coronal holes. Black lines show closed coronal loops. The green line denotes the intersection of the heliospheric current sheet with the plane of the sky. It is contained within two (dipolar) helmet streamers. A third "pseudostreamer" at the northern pole (top of the image) is produced by the convergence of open flux of the same polarity and thus does not contain a current sheet.

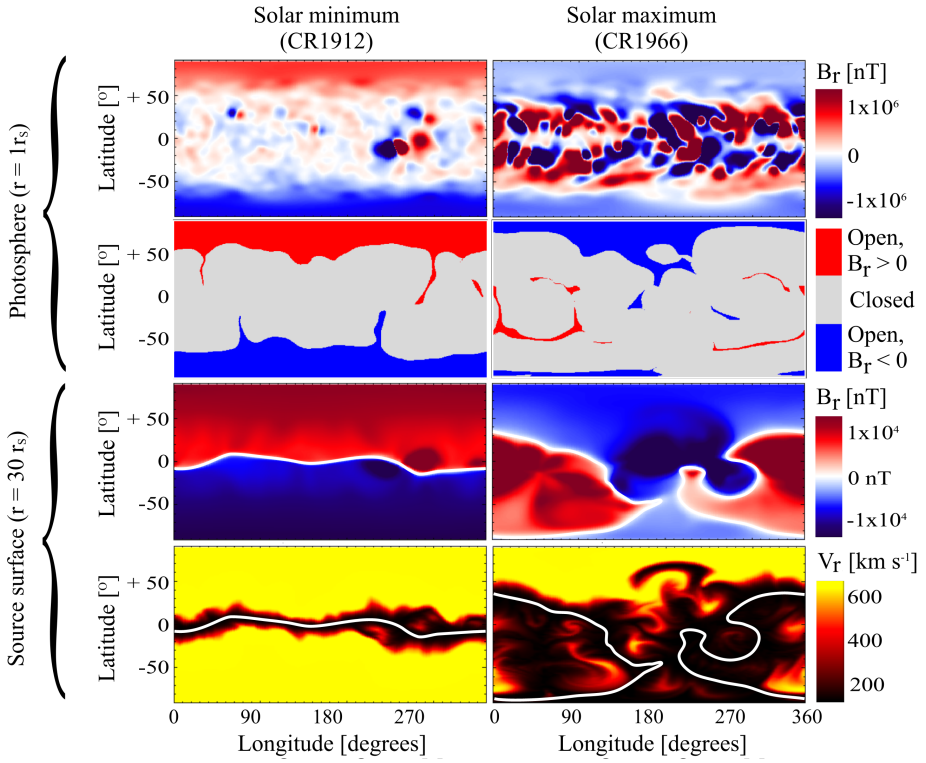

Figure 5: Examples of coronal MHD model solutions to the observed photospheric magnetic field during solar minimum (left) and solar maximum (right). Top: Observed B_r at the photosphere, smoothed and saturated to show the weak, large-scale fields as well as the intense active regions. Second row: The coronal hole map at the photosphere, with red/blue showing footpoints of open positive/negative flux and grey showing footpoints of closed flux. Third row: B_r at the outer model boundary (30 solar radii). Bottom: Solar-wind speed at 30 solar radii. In the bottom two rows, white lines show the location of the heliospheric current sheet. All data from http://www.predsci.com/mhdweb.

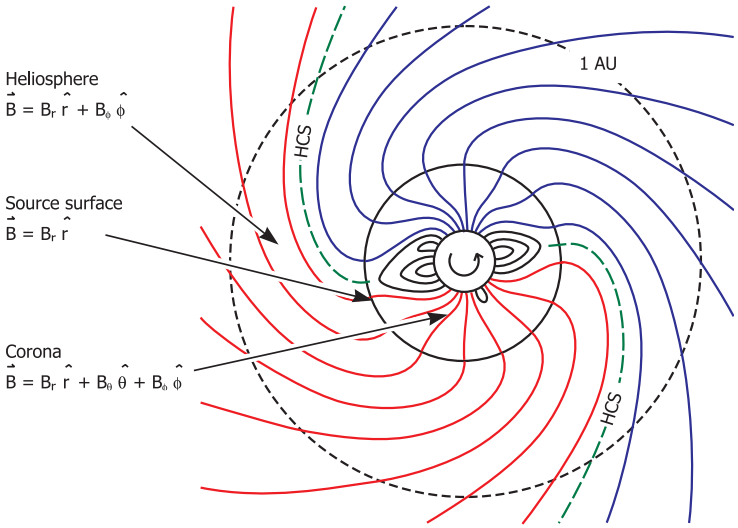

Figure 6: A sketch of the coronal and heliospheric magnetic field, looking down on the north pole of the Sun. In the corona, here shown bounded by the photosphere and a source surface, the magnetic field dominates the plasma flow and thus can form closed loops which prevent outflow. Thus the field undergoes significant non-radial expansion with height. By the source surface, typically taken to be a few solar radii, the solar-wind flow momentum dominates, and both the field and flow both become essentially radial. In the heliosphere, rotation of the HMF footpoints within a radial solar-wind flow generates an azimuthal component of the HMF, B_ϕ, leading to a spiral geometry. Regions of opposite HMF polarity, shown as red and blue lines, are separated by the heliospheric current sheet (HCS), shown as the green dashed line. Image adapted from [74] and [60].

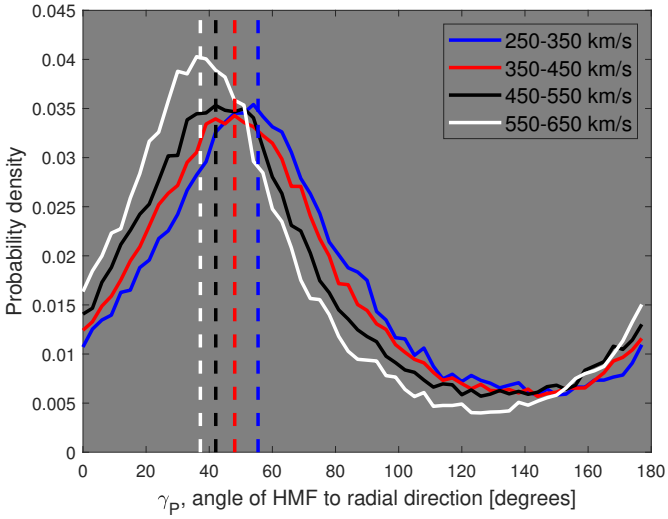

Figure 7: Occurrence in hourly spacecraft data of γ_P, the angle of the HMF to the radial direction, for different solar wind speed ranges. Vertical dashed lines show the ideal Parker spiral angle for the centre of the speed range. Updated from [60].

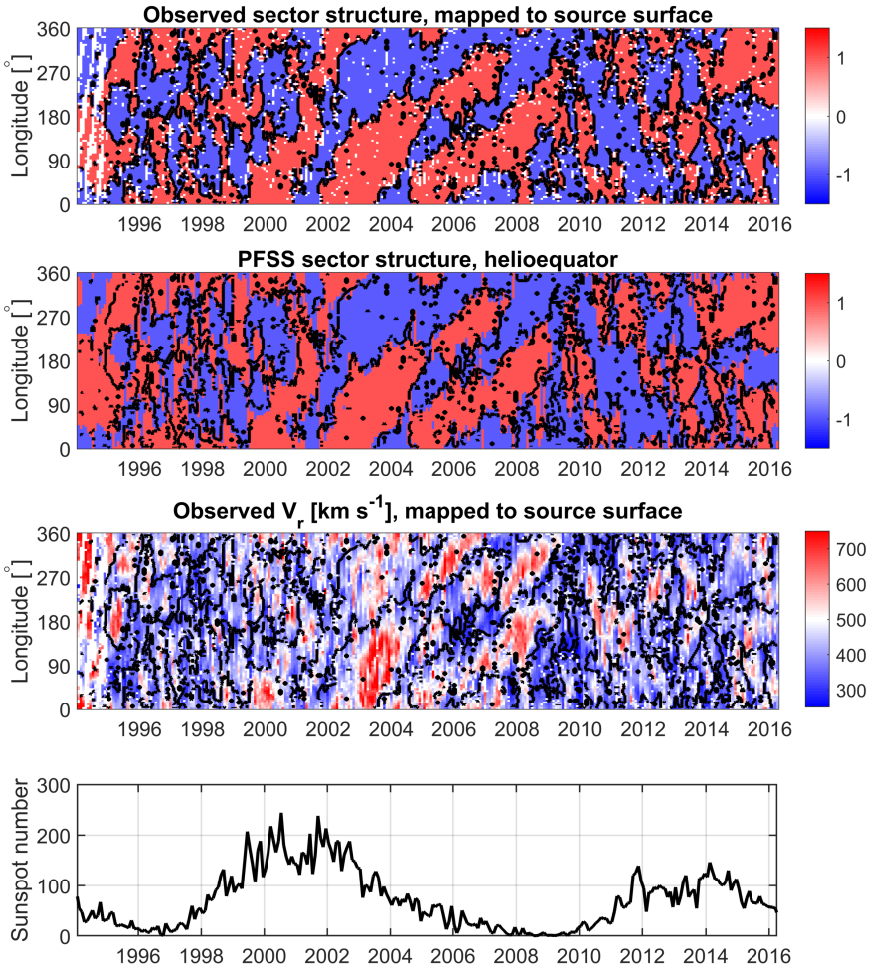

Figure 8: The observed *in situ* (top) and magnetogram-derived (2nd panel) ecliptic HMF polarity (or sector structure) as a function of solar longitude and time. Blue/red indicates inward/outward sectors, respectively. The third panel shows observed solar-wind speed, with red indicating fast and blue slow wind. In the top three panels the black dots show the observed HCS location. The bottom panel shows sunspot number. Updated from [60].

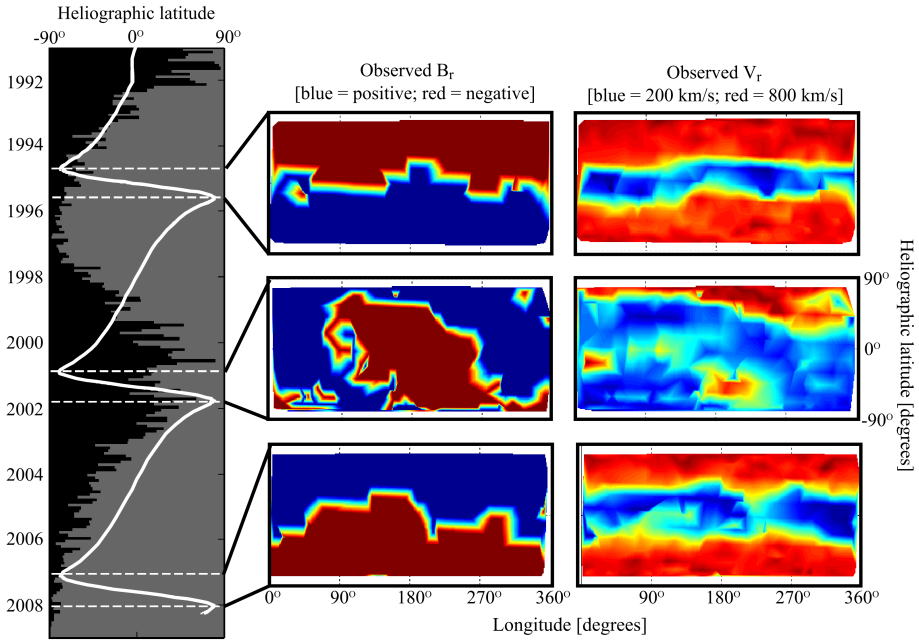

Figure 9: Solar-wind structure revealed by *in-situ* observations made by *Ulysses*. Left: Heliographic latitude of *Ulysses* (white), overlaid on sunspot number (black). The centre and right-hand columns show latitude-longitude maps of *Ulysses* observations made during the three fast-latitude scans. The centre column shows HMF polarity, with blue/red showing inward/outward HMF. The right-hand column shows solar wind speed, with blue through red showing 200 to 800 km s^{-1}. Image adapted from [61].

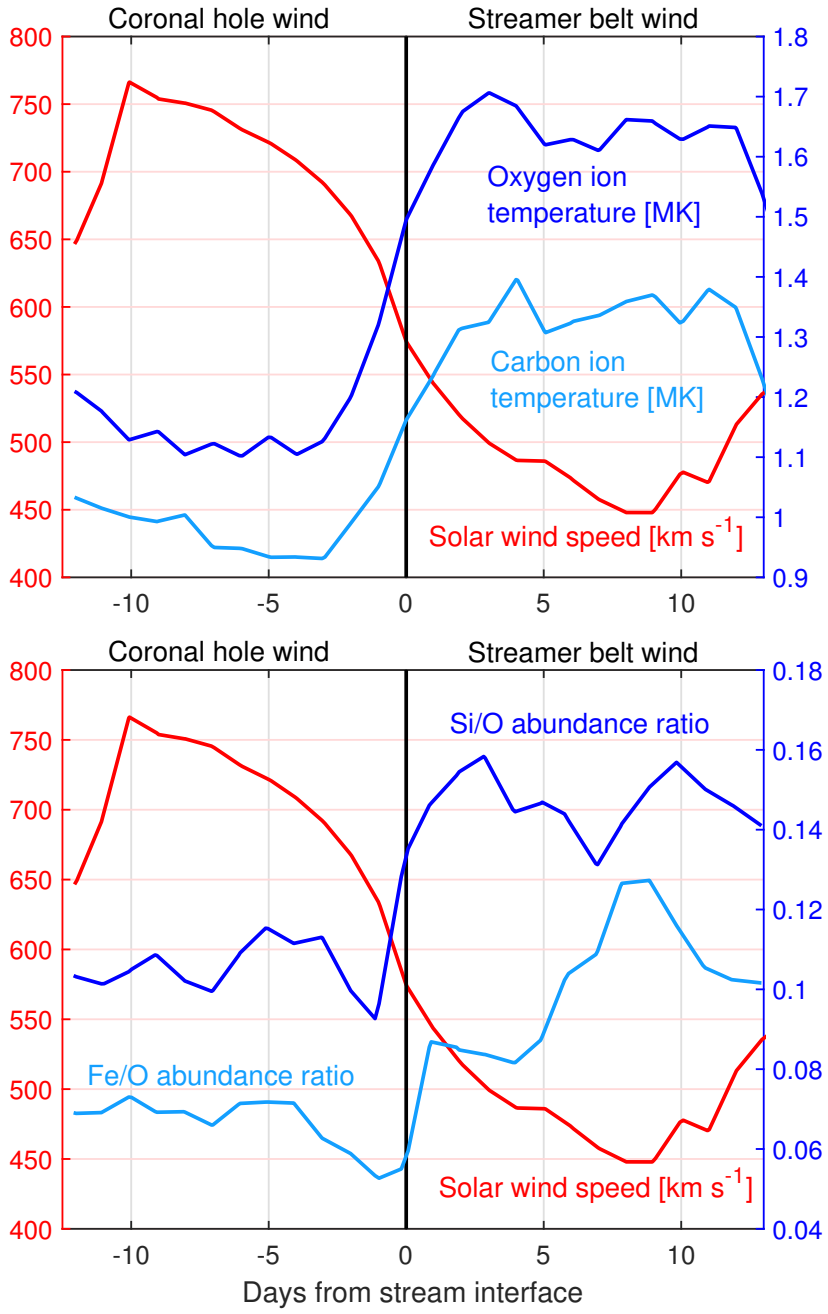

Figure 10: Solar-wind stream structure observed by *Ulysses*. The plot shows a composite (or super-posed epoch analysis) of 9 fast-to-slow wind transitions, with day 0 being the transition between the "fast" and "slow" streams. Top: Solar-wind speed (specifically, α speed) is shown by the red line. Thus fast wind from coronal holes is shown on the left, slow wind from the streamer belt on the right, though the transition is not obvious in solar wind speed. Blue lines show the coronal temperature associated with the observed oxygen and carbon ion charge states. Bottom: Elemental composition, in the form of the silicon-to-oxygen and iron-to-oxygen ratios. Adapted from [88]

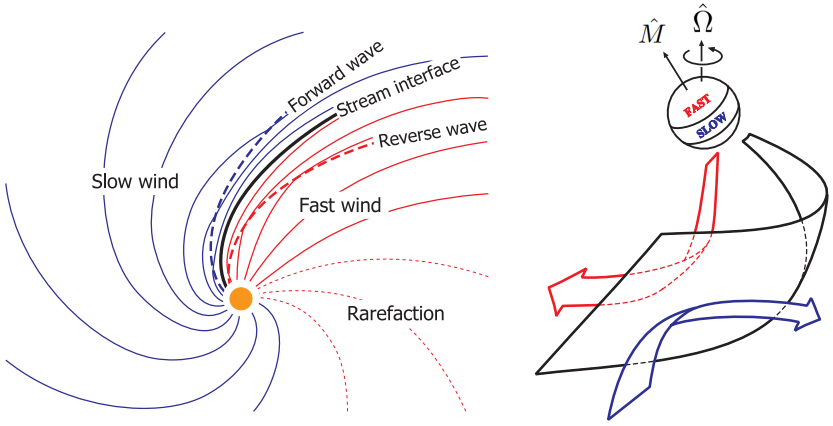

Figure 11: Schematics of stream interaction region formation. Left: Looking down on the solar equatorial plane. Magnetic field lines in fast/slow wind are shown in red/blue. The stream interface separates the fast and slow streams. Forward and reverse waves propagate out from the stream interface (SI) to accelerate the slow wind and decelerate the fast wind. Right: a view from Earth. The magnetic axis, $\hat{M}$, and thus the associated solar-wind speed structure, is inclined to the rotation axis, $\hat{\Omega}$. The SI forms a spiral front in the heliosphere, shown as the black-outlined curved surface. In the frame of reference of the SI, fast (red) and slow (blue) wind both flow toward the SI. Slow wind is deflected in the solar-rotation direction, while fast wind is deflected in the counter sense. This will produce a bipolar variation in the observed azimuthal component of the solar-wind velocity. Adapted from [60].

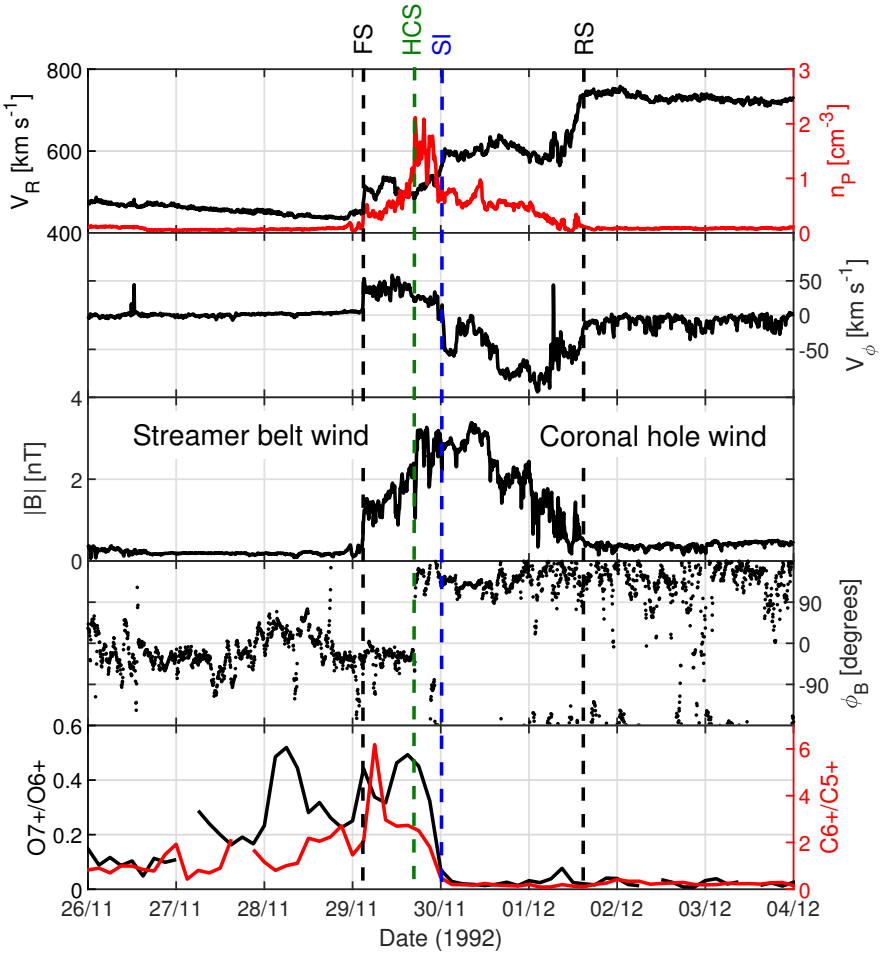

Figure 12: A stream interaction region observed by the *Ulysses* spacecraft just below the ecliptic plane (–20° latitude) at 5.1 AU. Panels from top to bottom show: radial solar-wind speed (black) and number density of protons (red); azimuthal solar-wind speed; HMF intensity; HMF angle to the radial direction; oxygen ion (black) and carbon ion charge-state ratio (red). Vertical black lines show the forward shock (FS) and reverse wave (RW); green shows the heliospheric current sheet (HCS) and blue shows the stream interface (SI).

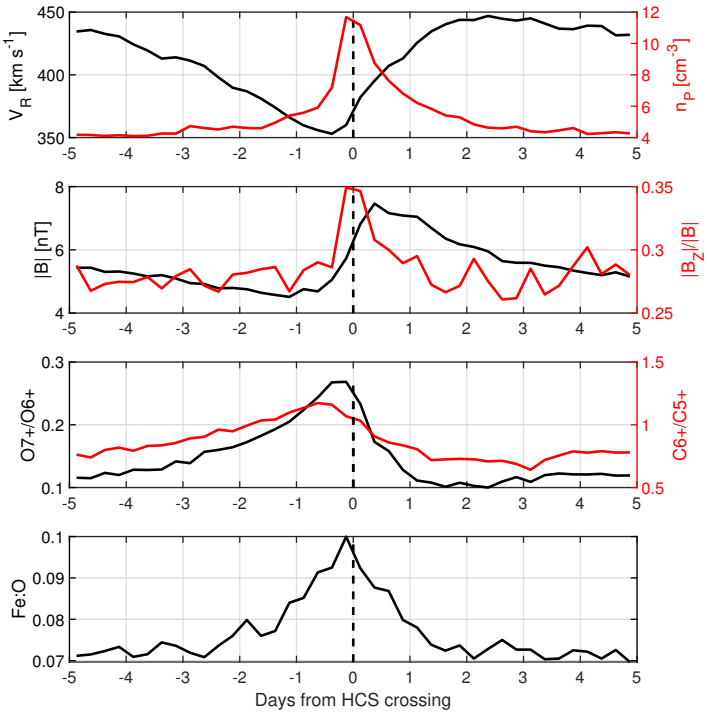

Figure 13: A super-posed epoch analysis of 307 heliospheric current sheet crossings observed by the ACE spacecraft in near-Earth space. Uncertainty bands have been omitted for clarity. Top: Radial solar-wind speed (black) and proton density (red). Second panel: HMF intensity (black) and fraction contributed by the out-of-ecliptic component, B_Z (red). Third panel: Oxygen (black) and carbon (red) ion charge-state ratios, which are a proxy for coronal source temperature. Bottom panel: The iron-to-oxygen occurrence ratio.

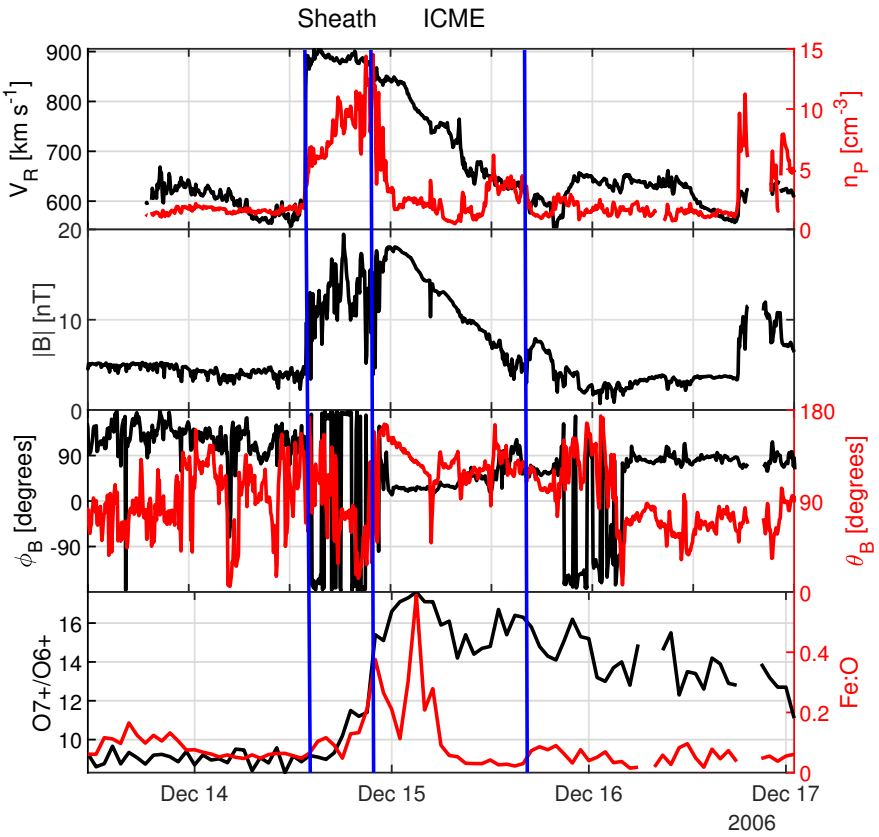

Figure 14: An interplanetary coronal mass ejection observed by the ACE spacecraft in near-Earth space. Panels from top to bottom show: radial solar-wind speed (black) and proton density (red); magnetic field intensity; HMF angle to the radial direction (black) and out of the ecliptic plane (red); oxygen ion charge-state ratio (black) and Fe:O ratio (red). Vertical blue lines show, from left to right, the times of the interplanetary shock, ICME leading edge and ICME trailing edge, respectively.

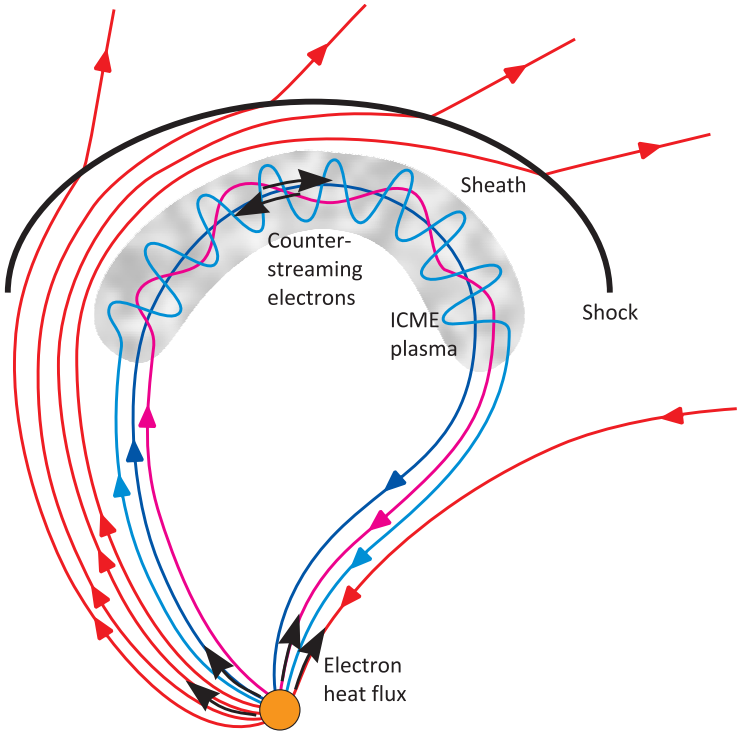

Figure 15: A schematic of the global structure of a "typical" interplanetary coronal mass ejection (ICME). Blue/purple lines show magnetic flux associated with the ICME, whereas red lines show the ambient heliospheric magnetic field. Black arrows indicate the direction of the suprathermal electron strahl. The hot, FIP-enhanced ICME plasma is threaded by a twisted magnetic flux rope, which is connected at both ends to the hot corona. The ICME drives an interpanetary shock, behind which the ambient solar wind is deflected and compressed. Reproduced from [58].

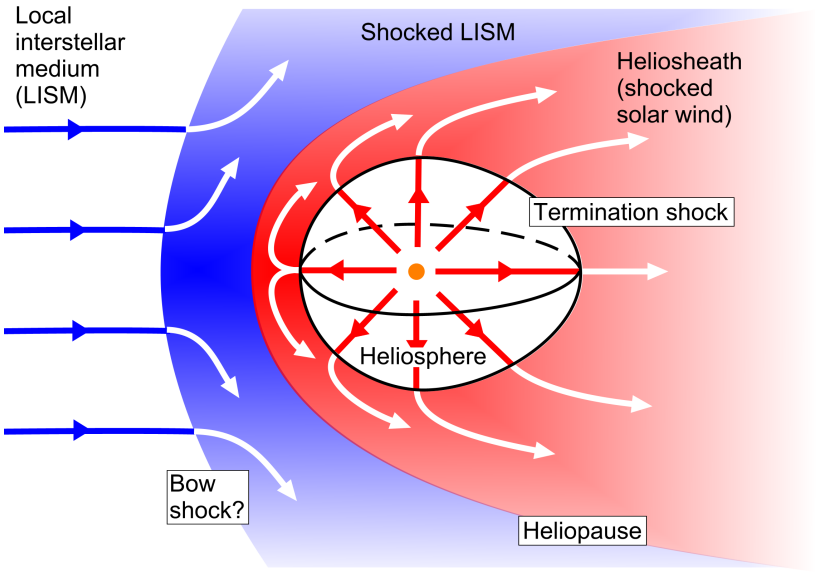

Figure 16: A schematic of the global structure of the heliosphere. The solar wind flows radially away from the Sun. As the flow is supermagnetosonic, a termination shock forms inside the heliopause, to slow and deflect the solar wind inside the heliosheath. Outside the heliopause, the local interstellar medium (LISM) is deflected around the heliosphere. Depending on the strength and orientation of the magnetic field within the LISM, this interaction may or may not involve a standing bow shock. Adapted from [60].